Helically Chiral Hybrid Cyclodextrin Metal-Organic Framework Exhibiting Circularly Polarized Luminescence

Masoud Kazem-Rostami, [§] Angel Orte, [+] Ana M. Ortuño, [¥] Arthur H. G. David, [§] Indranil Roy, [§] Delia Miguel, [+] Amine Garci, [§] Carlos M. Cruz, [¥] Charlotte L. Stern, [§] Juan M. Cuerva, [¥*] J. Fraser Stoddart *[,§,#,‡,£]

§ Department of Chemistry, Northwestern University, 2145 Sheridan Road, Evanston, Illinois 60208-3113, United States
+ Nanoscopy-UGR Laboratory, Departamento de Fisicoquimica, Facultad de Farmacia, Unidad de Excelencia de Química, University of Granada, Granada 18071, Spain
¥ Department of Organic Chemistry, Unidad de Excelencia de Química, University of Granada, Avda. Fuentenueva, Granada 18071, Spain
 # School of Chemistry, University of New South Wales, Sydney, NSW 2052, Australia
‡ Stoddart Institute of Molecular Science, Department of Chemistry, Zhejiang University, Hangzhou 310021, China
£ ZJU-Hangzhou Global Scientific and Technological Innovation Center, Hangzhou 311215, China

*E-mail: jmcuerva@ugr.es, stoddart@northwestern.edu

SUPPORTING INFORMATION

***Correspondence Address**	***Correspondence Address**
Professor Juan M Cuerva Department of Organic Chemistry Unidad de Excelencia de Química University of Granada Granada, 18071 (Spain) Tel: (+34) 958-243-319 E-Mail*: jmcuerva@ugr.es*	Professor J Fraser Stoddart Department of Chemistry Northwestern University 2145 Sheridan Road Evanston, IL 60208-3113 (USA) Tel: (+1) 847-491-3793 E-Mail: *stoddart@northwestern.edu*

Table of Contents

Section A. Materials and Methods

Materials

The starting materials of ReagentPlus© purity and HPLC-grade solvents were purchased from MilliporeSigma and Fisher Scientific, respectively, and used without further purification. Potassium deuteroxide (KOD) 40 *wt.*% solution in D_2O, and neat D_2O were purchased from Cambridge Isotope Laboratories (CIL). Compounds 1-pyrenecarboxylic acid, 9-anthracenecarboxylic acid, perylene-3,9-dicarboxylic acid and γ-cyclodextrin have been abbreviated to PyCA, AnCA, PeCA and γ-CD throughout this Supporting Information and Manuscript, and, in the ease of their conjugate carboxylates, to $PyC^–$, $AnC^–$, $PeC^–$, respectively.

Synthesis of Pristine CD-MOF-1

Adaption of the synthetic procedure reported[S1] by us earlier for the synthesis of CD-MOF-1 as follows: γ-CD (2.08 mg, 1.6 mmol) and KOH (718 mg, 12.8 mmol) were dissolved in HPLC-grade H_2O (32 mL). This aqueous solution was passed through a 0.2 μm microfilter and recollected in a nitrogen-flushed beaker. MeOH (40 mL) was allowed to diffuse slowly into the aqueous solution at RT over 10 days. Colorless cubic crystals were isolated, placed on a sintered filter and rinsed with a 1:3 blend of HPLC-grade H_2O–MeOH (3 × 5 mL), and then with pure MeOH (3 × 10 mL). The crystals were transferred to a high-vacuum chamber and dried at 30 ºC to afford activated CD-MOF-1 as white cubes (1.84 g, 66%).

Synthesis of Dye-Loaded CD-MOFs by Co-crystalization

γ-CD (2.08 mg, 1.6 mmol) and KOH (718 mg, 12.8 mmol) were dissolved in HPLC-grade H_2O (32 mL) and decanted into three separate 15 mL Falcon™ tubes, each receiving 10 mL of the solution. Each tube was charged with an excess (1.0 mmol) of one of the fluorophores and an additional amount of KOH (1.0 mmol for PyCA and AnCA, and 2.0 mmol for PeCA). The tubes were capped, sealed with Parafilm™ and sonicated at RT for 20 min. They were centrifuged at 5000 rpm for 10 min at RT and their solutions passed through a 0.2 μm microfilter before recollection in three separate nitrogen-blown vials. MeOH (15 mL) was allowed to diffuse gradually into the aqueous solutions at RT over 3 weeks. Highly fluorescent crystals

were isolated placed on a sintered filter and rinsed with a 1:3 blend of HPLC-grade H_2O–MeOH basified with 5% KOH (3 × 10 mL), and finally with pure MeOH (3 × 10 mL). The crystals were transferred to a vacuum chamber and dried at 30 ºC yielding 46, 52, and 31% of $AnC^–$, $PyC^–$, and $PeC^–$, as dye-loaded CD-MOFs, respectively. The relative ratios of $AnC^–$, $PyC^–$, $PeC^–$ to γ-CD (Table S1) were calculated based on ^1H NMR spectroscopic analysis of these digested MOFs.

Table S1. Ratios of the Fluorescent Guest Molecules to γ-CD Quantified by ^1H NMR Spectroscopic Analyses of the Digested CD-MOFs

Fluorophore	Ratio of fluorophore/γ-CD		
	Co-crystallization in mother liquor	Diffusion in mother liquor	Diffusion in MeOH
$AnC^–$	2.1:1.0	0.98:1.0	0.82:1.0
$PyC^–$	0.82:1.0	0.12:1.0	0.53:1.0
$PeC^–$	0.37:1.0	0.30:1.0	0.09:1.0

The solvents used for rinsing the MOFs were combined with the corresponding mother liquors from the syntheses step and subjected to rotary evaporation to remove MeOH. The remaining aqueous solutions were then transferred to new Falcon tubes. The contents of the tubes were acidified with conc. HCl and left to cool down to RT, before being centrifuged at 5000 rpm for 10 min. The top clear solution mainly containing NaCl was discarded. The remaining solids were rinsed with cold deionized H_2O and dried under a high vacuum to recover the pure dyes.

Synthesis of Dye-Loaded CD-MOFs by Diffusion

Adaption of procedures from earlier investigations by us[S2] suggest—for the maximum inclusion of guests molecules in the CD-MOFs—involved minor modifications as follows: An excess of each fluorophore (1.0 mmol) and KOH (1.0 mmol for PyCA and AnCA, and 2.0 mmol for PeCA) were placed in separate vials and H_2O (1 mL) was added. The vials were capped and sonicated until the solution were homogenous, after which MeOH (5 mL) was added. The solutions were passed through 0.2 μm microfilters and poured over freshly activated CD-MOF-1 crystals (100 mg) kept in separate nitrogen-flushed vials. In parallel fashion, the same amount of each fluorophore (1.0 mmol) and KOH (1.0 mmol for PyCA and AnCA, and 2.0 mmol for PeCA) were added to the mother liquors (6 mL) in a vial containing as-synthesized CD-MOF-1 crystals (100 mg). The vials were capped and dark-incubated so as to keep the crystals immersed for 2 weeks at RT to equilibrate. The resulting fluorescent crystals were then isolated and placed on a sintered filter, before being rinsed with a 1:3 mixture of H_2O–MeOH (3 × 10 mL), followed by HPLC-grade MeOH (3 × 10 mL). A few crystals from each batch were transferred to a vacuum oven and dried at 30 ºC before being digested and subjected to ^{1}H NMR spectroscopic analysis in D_2O so as to obtain the ratios (Table S1) of AnC^-, PyC^-, PeC^- to γ-CD. The remaining mother liquors and dye-contaminated solutions were

combined and recycled as described previously in order to retrieve the unused fluorophores.

X-Ray Diffractometry

A suitable $PyC^{-}\subset$CD-HF crystal was selected and mounted on a MITIGEN holder with Paratone oil on a XtaLAB Synergy, Single source at home/near, HyPix diffractometer. The crystal was kept at 100.03(10) K during data collection. Using Olex2,[S3] the structure was solved with the ShelXT[S4] structure solution program using Intrinsic Phasing and refined with the XL[S5] refinement package using Least Squares minimisation. For the other crystals, Rigaku Cu-Synergy X-ray diffractometer was used to collect crystallographic data which was processed and refined with Olex2 showing the typical CD-MOF-1. Stoe STADI-MP, running on pure $K\alpha_1$ radiation of Cu-sealed tube was used for the collection of high-resolution powder diffraction data.

NMR Spectroscopy and Titrations

NMR Spectra were recorded at 298 K on (i) Bruker Avance III 600 MHz, (ii) Bruker Neo 600 MHz, and (iii) Bruker Avance III 500 MHz spectrometers employing the following software programs: Topspin version 4.0.8 and MestReNova version 14 for the analysis and plotting of the acquired spectra. CD-MOFs were rinsed thoroughly with a 1:1 mixture of MeOH and 1M aqueous KOH solution and then with cold MeOH before being dried under high vacuum at 40°C/1h. The dried CD-MOFs were dissolved in KOD (3.9 ± 0.6 %) solution in D_2O to assist the solubility

of the components and achieved consistency of the pH prior to recording NMR spectra.

Stock solutions of the corresponding carboxylic acid (PyCA, AnCA, PeCA) in a solution of KOD (≈ 3.9 %) in D_2O were prepared ahead of carrying out the titrations. A solution of γ-CD was also prepared in a separate vial using the stock solution of the corresponding carboxylic acid as a solvent in order to maintain a constant concentration of the corresponding carboxylic acid during titrations. The addition of γ-CD solutions to solutions of the carboxylic acid (500 μL) were achieved with Hamilton® syringes using the following order: 7 × 15 μL, 4 × 30 μL, 5 × 50 μL. After each addition, the solutions were shaken for 20 secs and the ^{1}H NMR spectra were recorded. In order to determine the association constants between the carboxylic acids and γ-CD, the analysis of ^{1}H NMR spectroscopic data was carried out using a nonlinear least-squares curve fitting procedure performed with the online software Bindfit (http://supramolecular.org/) with a 1:1 global fitting model[S6] (Nelder-Mead method).

Steady-State and Time-Resolved Fluorescence Spectroscopy

Steady-state and time-resolved luminescence spectroscopy of $PyC^{-}\subset$CD-HF crystals were performed on a Horiba QuantaMaster 8000 equipped with a specific cell holder for solid-state samples. As excitation sources, we used a Xe lamp for steady-state measurements and a pulsed 340-nm NanoLED, working at a repetition

rate of 0.5 MHz, for time-resolved measurements. Absolute luminescence quantum yield values were estimated with an integrating sphere. In the case of all these measurements, a small amount of $PyC^{-}\subset$CD-HF crystals was dispersed, mixed, and ground with $BaSO_4$. Time-resolved emission spectroscopy (TRES) of $PyC^{-}\subset$CD-HF suspended in MeOH was carried out in a PicoQuant FluoTime 200 fluorimeter, equipped with a 375-nm pulsed diode laser, working at a frequency of 2.5 MHz collecting 24 fluorescence decay traces in the 390–620 nm emission range ($\Delta\lambda_{em}$ = 10 nm) during a fixed time (500 s) in order to maintain the overall intensity information. In the case of TRES analyses and the estimation of the species-associated emission spectra (SAEMS), the fluorescence decay traces were fitted to a three-exponential function using a Levenberg-Marquard algorithm-based nonlinear least-squares error minimization iterative reconvolution method (FluoFit 4.4 package, PicoQuant GmbH). The 24 decay traces were fitted globally with the decay times linked as shared parameters, whereas the pre-exponential factors were local adjustable parameters. The quality of fittings was assessed by the value of the reduced chi-squared (χ^2) parameter and random distributions of the weighted residuals and the autocorrelation functions. The SAEMS of each species *i* at any given emission wavelength ($SAEMS_i(\lambda_{em})$) was calculated from the fluorescence intensity emitted by the species *i* ($A_{i,\lambda em}\times \tau_i$), normalized by the total intensity and

corrected for the different detection sensitivity using the total intensity of the steady-state spectrum ($I_{ss,\lambda em}$):

$$SAEMS_i(\lambda_{em}) = \frac{A_{i,\lambda em} \times \tau_i}{\sum_i A_{i,\lambda em} \times \tau_i} \cdot I_{ss,\lambda em} \qquad \text{(eq. S1)}$$

The approximate contribution of each species can be assessed as the area under the SAEMS. Since the initial amount of each form in the excited state (after the pulse excitation) is unknown, the estimation assumes an equal excitation rate for all the species.

Fluorescence Lifetime Imaging Microscopy (FLIM)

Fluorescence lifetime imaging microscopy (FLIM) was performed on a MicroTime 200 system (PicoQuant GmbH, Germany) based on an Olympus IX-71 inverted confocal microscope (Olympus, Japan). The excitation source was a 375 nm pulsed diode laser working at a repetition rate of 5 MHz. The collected fluorescence emission was filtered by a 405 nm long-pass filter after the main dichroic and before the 75-μm confocal aperture. Then, the emission was detected[S7] in an avalanche silicon photodiode (SPCM-AQR-14, Perkin-Elmer) after being filtered by a 520/35 bandpass filter (Chroma). FLIM images of individual dry crystals of $PyC^{-}\subset$CD-HF or crystals suspended in MeOH were collected with a 512×512 pixel resolution and a dwell time of 60 μs/pixel. In the case of spectroscopic information, the system was

equipped with an Andor Shamrock 303i-A spectrograph and an ultrasensitive Andor Newton electron-multiplying CCD (EM-CCD) camera. The spectra were obtained by pointing the excitation laser into different regions within the crystals, after having pre-scanned a specific area. The emitted luminescence was diverted to a fiber coupler and an F-matcher after the pinhole. The spectrograph held a 1200-line/mm grating to disperse the collected photons at different wavelengths and focus them onto the pixels of the EM-CCD camera. The luminescence spectra were collected with 5 accumulations of 0.5-s readouts, with a wavelength resolution of 0.351 nm. In order to reduce random noise in the spectra, a 5-point Fast Fourier Transform smoothing filter was applied using OriginPro 8.6 (OrginLab Co.). FLIM images were analyzed employing SymphoTime 64 software (PicoQuant GmbH, Germany). All images were spatially pre-binned with a 2×2 pixel window, and subsequently fitted with a two-exponential decay function. Luminescence lifetime distributions of the two decay times were extracted from pixels containing crystals. In the case of $PyC^{-}\subset$CD-HF crystals in the solid-state or suspended in MeOH, the short decay time exhibited (Figure S28b) a negative pre-exponential factor, indicating the presence of dynamic excimer formation during the time span of the excited state. DYNEX Image filtering was applied[S7] to identify regions where the excited state kinetics were more notable (Figure S28c).

Circularly Polarized Luminescence (CPL) Measurements

Both emission and CPL measurements were performed on an Olis DSM172 spectrophotometer using a 1.0 cm path-length quartz cell and a fixed wavelength LED (300 nm) as the excitation source. Collected crystals were washed with fresh HPLC-grade MeOH between 3 and 5 times on a vacuumed filter and then dried under an inert atmosphere. The solid material was ground to a homogeneous powder which, subsequently, was suspended in HPLC-grade MeOH. When measuring emissions, a 0.01 s integration time was selected, while, for CPL, 0.5 s integration time was used. CPL Measurements were collected by accumulating 200 scans and homogenizing the sample before each scan. In order to prove the absence of photoselection in these measurements, this procedure was repeated according to a method developed by Dekkers et al.[S8] It requires perpendicular excitation and emission channels (as is the case here) and a horizontally polarized incident radiation. Under this configuration, the signal obtained is similar to the original one using unpolarized excitation.

Electronic Circular Dichroism (ECD) Measurements

Both absorbance and ECD measurements were performed using a 10 mm path-length quartz cells and Olis DSM172 spectrophotometer. Although ECD measurements are a common approach for checking the reliability of CPL, exceptions apply. One exception relates to dynamic systems, such as excimers,

whose chirality is only present in the excited state and hence is undetectable[S9] by ECD. We had to first of all confirm that the chirality originates mainly from a static excimer. This confirmation requires the dimer to pre-exist in the ground state where ECD can be optimal. Suspensions were opaque—the light reaching the detector was null—and hence did not produce a reliable baseline or consistent reference. In addition, once the solids have been decanted, the signal from the solution is no longer related to the solids as confirmed by FLIM measurements that prove unequivocally that the (static)excimer-like emission only originates from the solid, See Figure 4 in the main text. The use of clearer solutions is not a reliable method either since inhomogeneous systems do not obey the Lambert-Beer´s law, resulting in a significant reduction of the signal intensity from CD-HF crystals suffering much interference from the PyC^- anions which have leaked out of CD-HF crystals. In fact, the only signal observed in UV-Vis spectra originates from monomeric species in the solution that does not present any ECD. Despite our attempts employing various experimental setups, no reliable ECD was observed in the (static)-excimer region for the suspension. CD-HF crystals are brittle and their deposition as thin films is not possible. This brittleness disables the direct acquisition of ECD from thin films. We, therefore, dispersed the sample in Nujol—in which the sample is stable—and sandwiched the resulting dispersion between two KBr disks. This dispersion, despite its good stability, was opaque. Because of the high moisture content of this type of

MOF our attempts at preparing KBr pellets with an evacuable KBr die and hydraulic press also failed. Despite all our efforts, no reliable ECD spectra were obtained. In order to avoid any misleading interpretation of our findings in absence of ECD, we checked the reliability of the CPL signal following an alternative method recommended[S10] in the literature along with the use of theoretical calculations. The results of these theoretical calculations are in excellent agreement with the observed CPL values.

Theoretical Calculations

Time-dependent density functional theory (TD-DFT) calculations were performed using the Gaussian16 suite. In order to simulate the UV and ECD spectra, the geometry of the two PyC^- present in the $(\gamma\text{-CD})_2$ tunnel was taken from the X-ray diffraction structure and the first 30 electronic transitions were calculated at the CAM-B3LYP /6-31G(d) level of theory. The UV and ECD spectra were represented (Figure S29 and S30) with a peak half-width at half-height of 0.2 eV. The theoretical g_{abs} value of the lowest energy transition was calculated from the module of the electric and magnetic transition dipole moments according to the following equation:

$$g_{abs} = \frac{4|\mu||m|\cos\theta_{\mu,m}}{|\mu|^2+|m|^2} = \frac{4R}{D+G} \quad \text{(eq. S2)}$$

where |μ| is the module of the electric transition dipole moment, |m| is the module of the magnetic transition dipole moment and θ the angle between them. R is the

rotatory strength, D the electric dipole strength ($D = |\mu|^2$) and G the magnetic dipole strength ($G = |m|^2$). The g_{abs} value for the lowest energy transition was calculated as +0.0023.

In order to obtain the theoretical g_{lum} value of the $S_1 \rightarrow S_0$ transition, the geometry optimization of the S_1 excited state of the γ-CD–PyC^-–PyC^- is required. The geometrical optimization of the S_1 excited state of the entire supramolecular system is not feasible by employing a reliable density function and basis set, since they require a tremendous amount of computation. Additionally, the optimization of the S_1 excited state of the two PyC^- molecules, subtracting the γ-CD moiety, afforded geometries that would not match the space available in the $(\gamma\text{-CD})_2$ tunnel. Therefore, constrictions were applied to the initial geometry (taken from the X-ray superstructure) with the coordinates of the carboxylates ($PyCO_2^-$) as well as their opposite aromatic carbon of each PyC^- frozen to simulate the effect of the $(\gamma\text{-CD})_2$ tunnel, and the geometry of the S_1 excited state optimized at the CAM-B3LYP/6-31G(d) level of theory. A single transition was calculated (Figure S31) at 441.05 nm, similar to the one obtained experimentally (480 nm). From the modules of the electric transition dipole moment and magnetic transition dipole moment, the calculated g_{lum} value of the $S_1 \rightarrow S_0$ transition was estimated (Figure S32) to be +0.0022, which is similar in sign and order to the experimental one (+0.0035) and also in accordance with the calculated g_{abs} value (+0.0023).

Table S2. Calculated Wavelengths, Oscillatory Strength (f), and Rotatory Strength (R) for the First 30 Electronic Transitions of the PyC^{-}– PyC^{-}

Transition number	Wavelength (eV)	Wavelength (nm)	Oscillatory Strength (f)	Rotatory Strength (R)
1	2.9940	414.10	0.0376	30.0726
2	3.0970	400.33	0.0431	–30.666
3	3.4052	364.10	0.0018	–6.9647
4	3.4402	360.39	0.0341	–2.3946
5	3.4823	356.04	0.0020	2.3729
6	3.5430	349.94	0.0473	–16.3796
7	3.6559	339.14	0.0019	–2.2256
8	3.7962	326.60	0.0033	–2.8199
9	3.8189	324.66	0.0185	–15.8955
10	3.8693	320.43	0.0143	3.1279
11	3.8844	319.18	0.0262	–21.1323
12	3.9624	312.90	0.0125	4.7373
13	4.0275	307.85	0.0020	0.4599
14	4.0724	304.45	0.0499	9.9583
15	4.0953	302.75	0.0260	32.7679
16	4.1086	301.77	0.0258	–7.4713
17	4.1278	300.36	0.0032	13.2034
18	4.1448	299.13	0.0043	6.7215
19	4.2117	294.38	0.0021	1.1959
20	4.3618	284.25	0.0100	–7.6242
21	4.4510	278.56	0.0007	–1.8604
22	4.4632	277.79	0.0017	1.0685
23	4.5085	275.00	0.0026	–2.3223
24	4.5345	273.42	0.0769	16.9969
25	4.5657	271.56	0.0110	20.1084
26	4.5842	270.46	0.0254	–15.0388
27	4.6027	269.38	0.0198	4.3221
28	4.6850	264.64	0.0148	–21.6827
29	4.7215	262.60	0.0041	13.5578
30	4.7469	261.19	0.0028	–0.347

Coordinates of the Optimized S_1 State

O	4.84649800	2.07655700	0.67168600
O	4.12169600	1.14773400	–1.19585400
C	2.55747000	1.44952500	0.67514200
C	2.56331800	1.11495700	2.03080500
H	3.52883500	0.92234700	2.48312500
C	1.39319600	1.04868200	2.76107500
H	1.41374800	0.75234000	3.80803000
C	0.16590700	1.37186200	2.17303000
C	–1.06848300	1.34117200	2.90021600
H	–1.04204400	1.01838600	3.93862600
C	–2.24035200	1.68745000	2.31949400
H	–3.17300300	1.64093600	2.87582900
C	–2.28922500	2.10154200	0.94576600
C	–3.48206600	2.47406900	0.32293900
H	–4.41078000	2.43934200	0.88701600
C	–3.48202200	2.86326600	–1.00654900
H	–4.42185100	3.14068800	–1.47999700
C	–2.31161300	2.89789300	–1.74723300
H	–2.33125300	3.19457100	–2.79318200
C	–1.09834800	2.52828900	–1.16832100
C	0.13180500	2.52198400	–1.90828800
H	0.09508000	2.79884400	–2.95972700
C	1.29510400	2.14161900	–1.33703100
H	2.23035800	2.07202300	–1.88272700
C	1.34594200	1.76531000	0.05055000
C	0.14571700	1.75377600	0.80825400
C	–1.08350900	2.12925300	0.19590300
C	3.88540800	1.55175800	–0.01787600

O	–4.81053700	–2.43906100	–0.19762900
O	–3.84137900	–1.78032600	1.73077700
C	–2.64724400	–1.57802500	–0.32474500
C	–2.85084200	–1.19332500	–1.66713700
H	–3.87077800	–1.02306700	–1.99691100
C	–1.81208900	–1.00059600	–2.53114500
H	–1.98897100	–0.64991400	–3.54536800
C	–0.47163900	–1.23151200	–2.10707900
C	0.62644200	–1.02317700	–2.97152100
H	0.42514500	–0.63895700	–3.97040800
C	1.91218600	–1.26289800	–2.57387400
H	2.74966000	–1.05188500	–3.23215600
C	2.18955300	–1.77272200	–1.27879100
C	3.50417400	–2.06468300	–0.86493100
H	4.32817600	–1.81718200	–1.52481500
C	3.73278000	–2.58585300	0.39313600
H	4.75499500	–2.79700000	0.70339100
C	2.69252800	–2.81977900	1.28342200
H	2.89261800	–3.21674000	2.27640700
C	1.36496500	–2.51168100	0.92813400
C	0.26627900	–2.70541200	1.79949200
H	0.45449200	–3.11818300	2.78861400
C	–1.01869100	–2.38317600	1.42277600
H	–1.82376900	–2.55940500	2.12275200
C	–1.31958600	–1.85977500	0.14403500
C	–0.23293400	–1.68746100	–0.77982200
C	1.10533700	–1.99037100	–0.37874800
C	–3.85961500	–1.92969100	0.41386800

Section B. NMR Spectroscopy

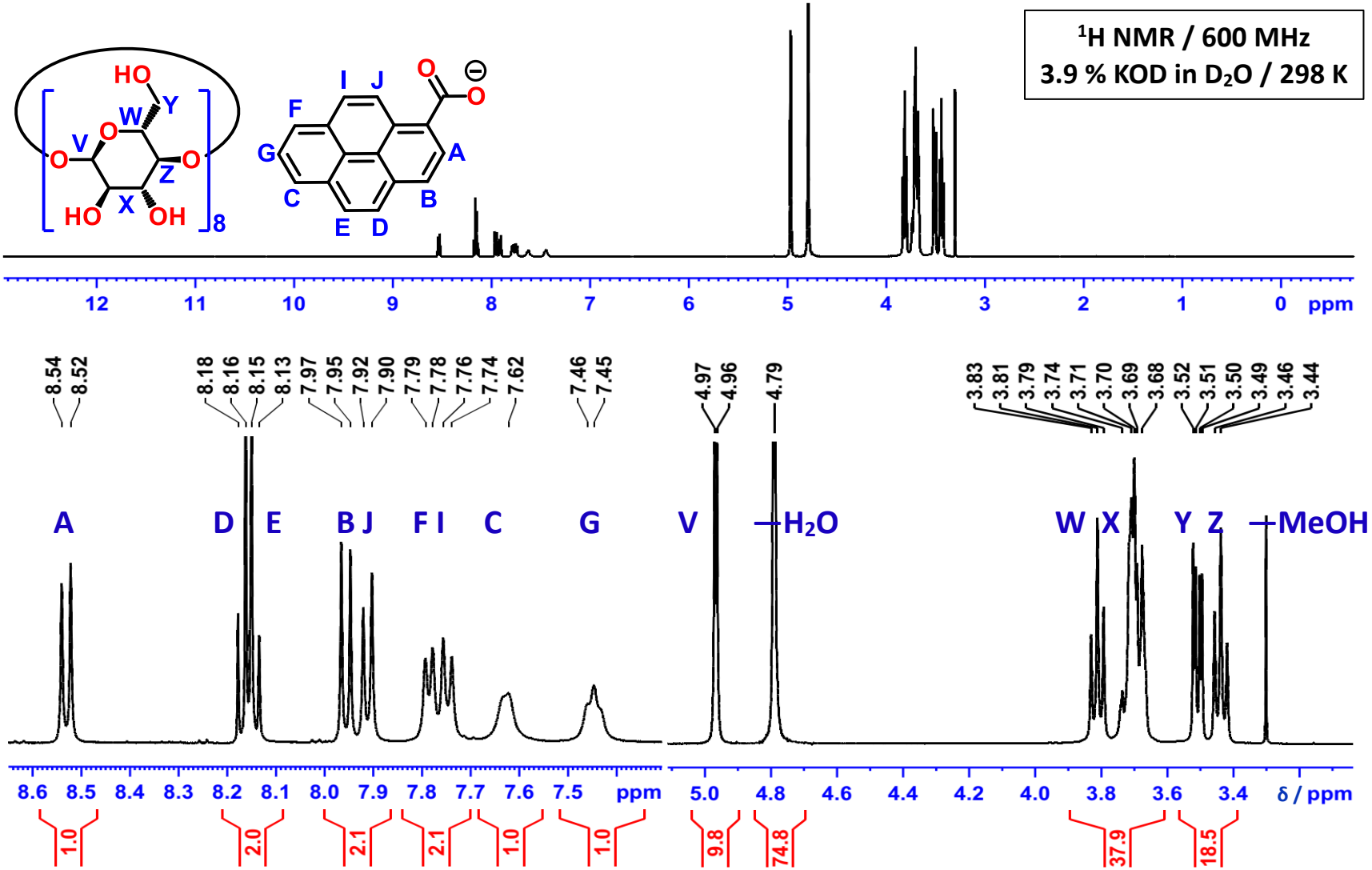

Figure S1. ^{1}H NMR spectrum of PyC^{-}⊂CD-HF co-crystal dissolved in D_2O

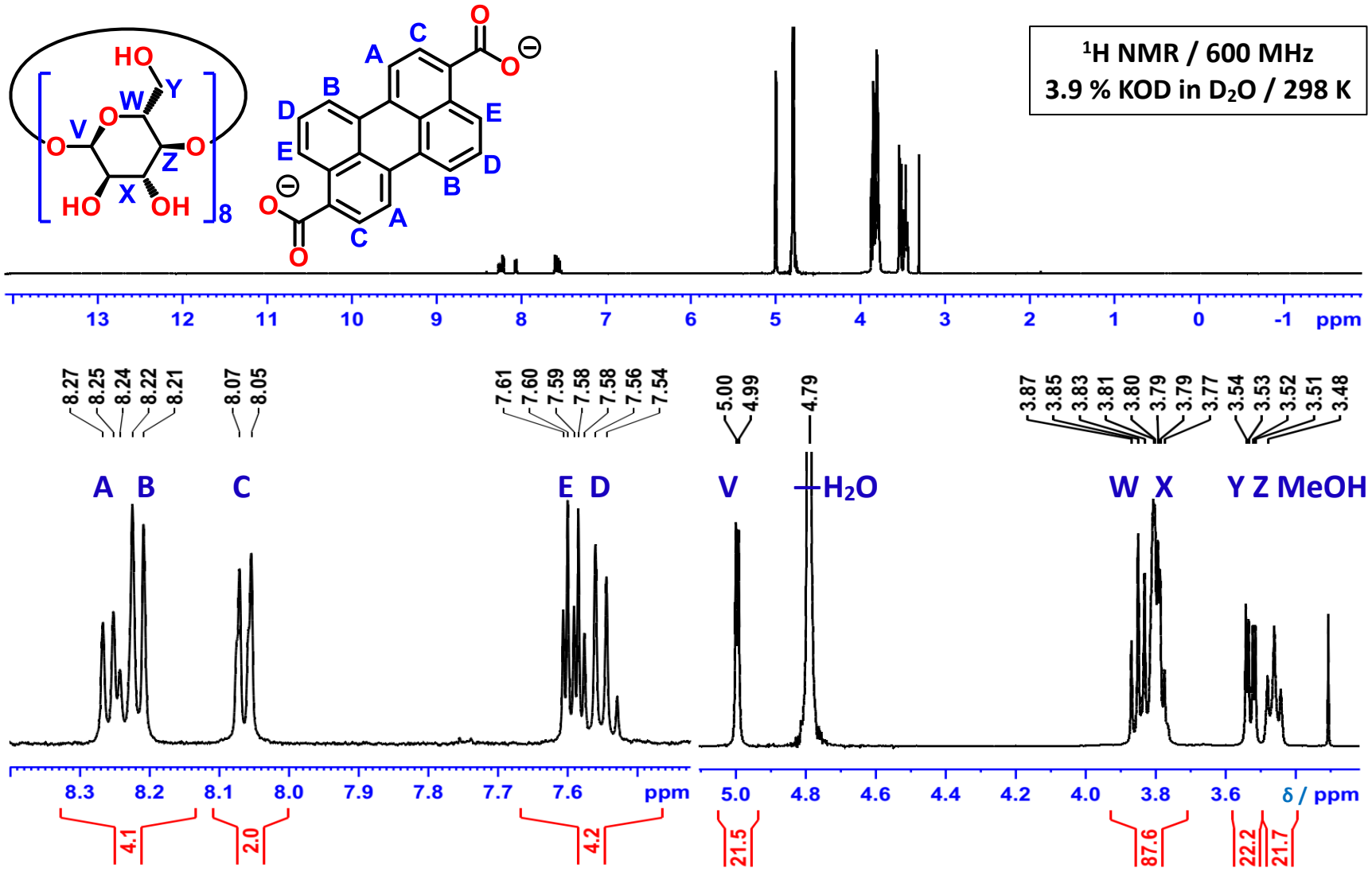

Figure S2. ^{1}H NMR spectrum of PeC^{-}⊂CD-MOF-1 co-crystal dissolved in D_2O

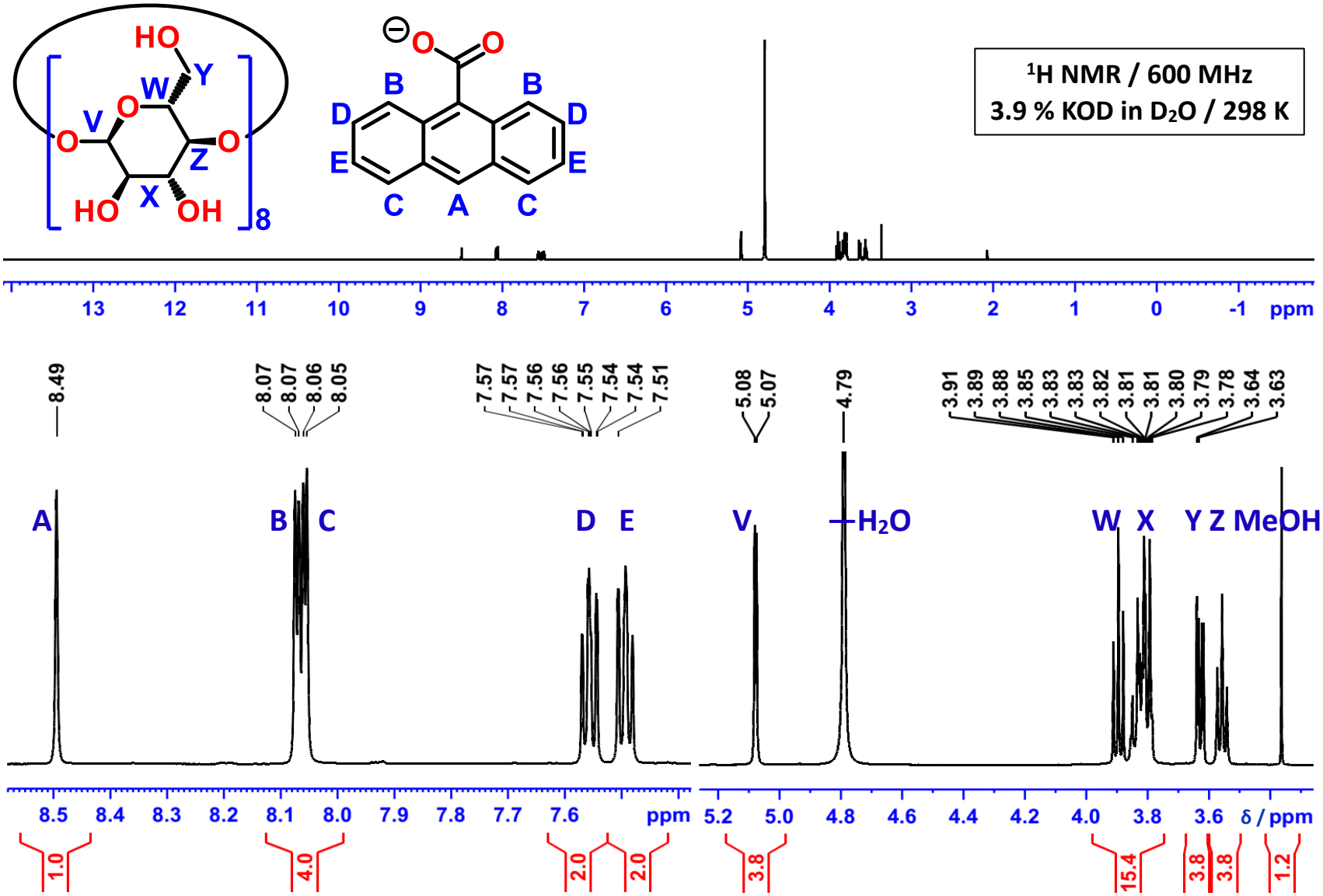

Figure S3. ^{1}H NMR spectrum of AnC^{-}⊂CD-MOF-1 co-crystal dissolved in D_2O

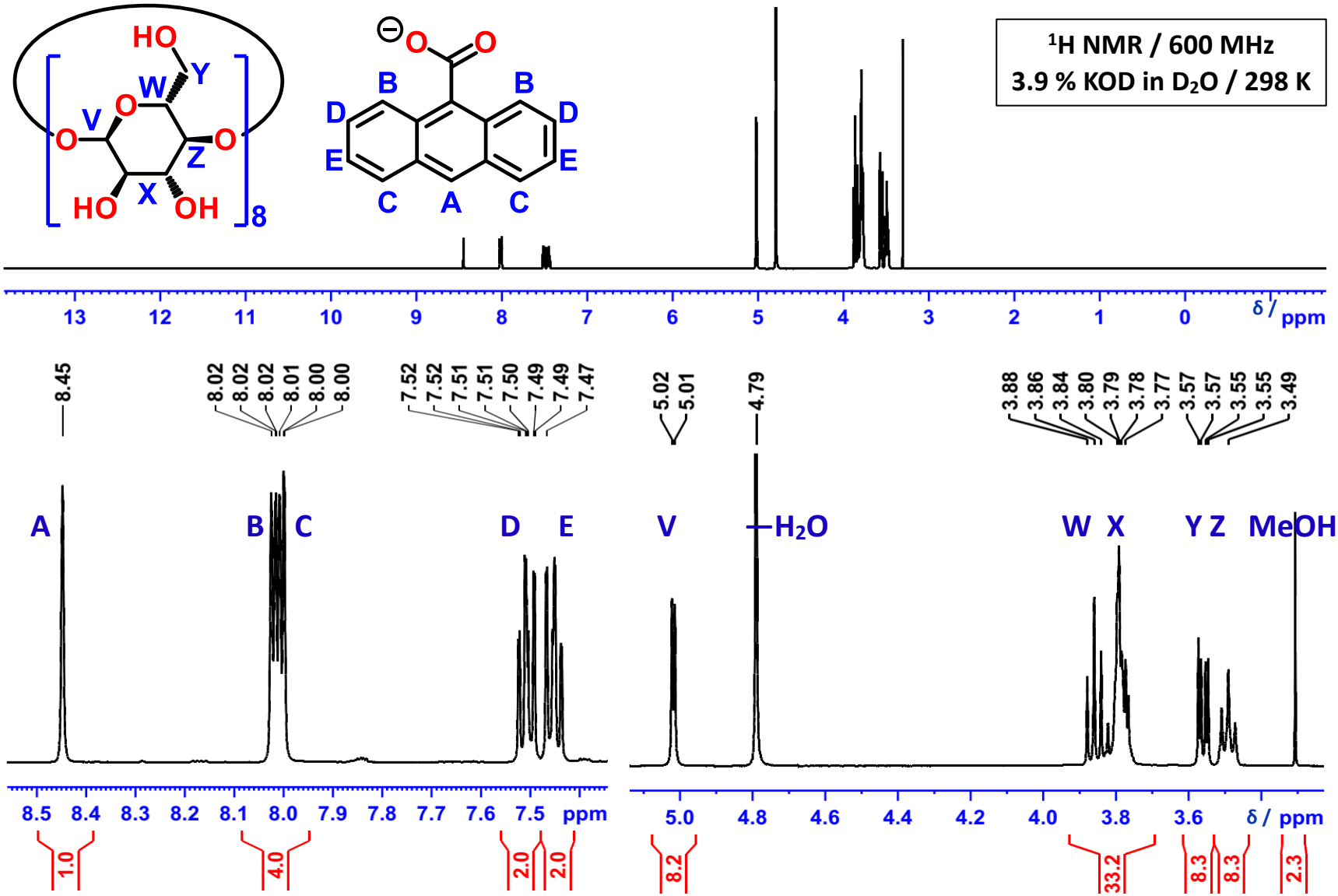

Figure S4. ^{1}H NMR spectrum of AnC^{-}⊂CD-MOF-1 diffused crystal dissolved in D_2O

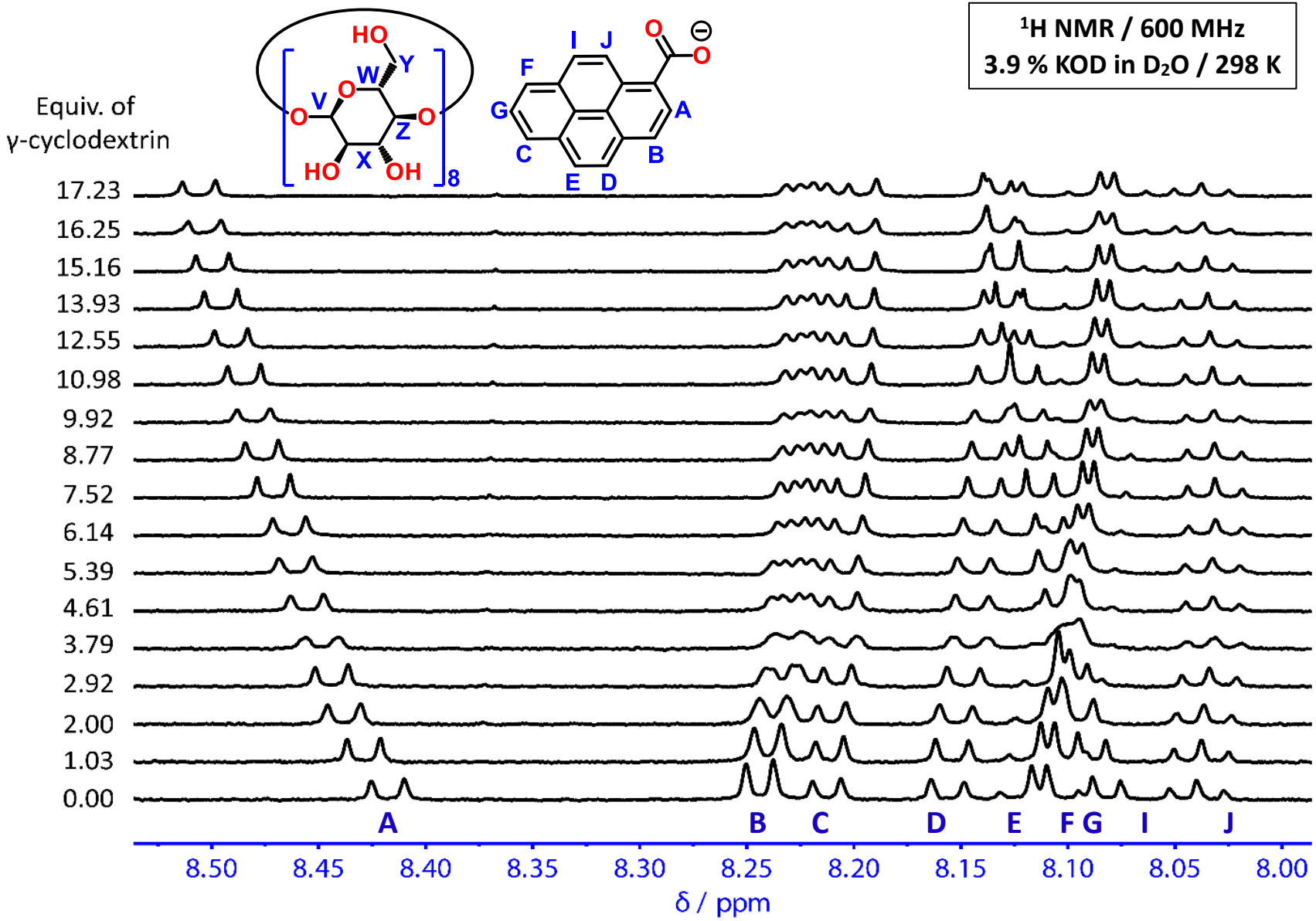

Figure S5. Stacked partial ^{1}H NMR spectra for the titration of PyC^{-} with γ-CD (0 – 17.23 equiv)

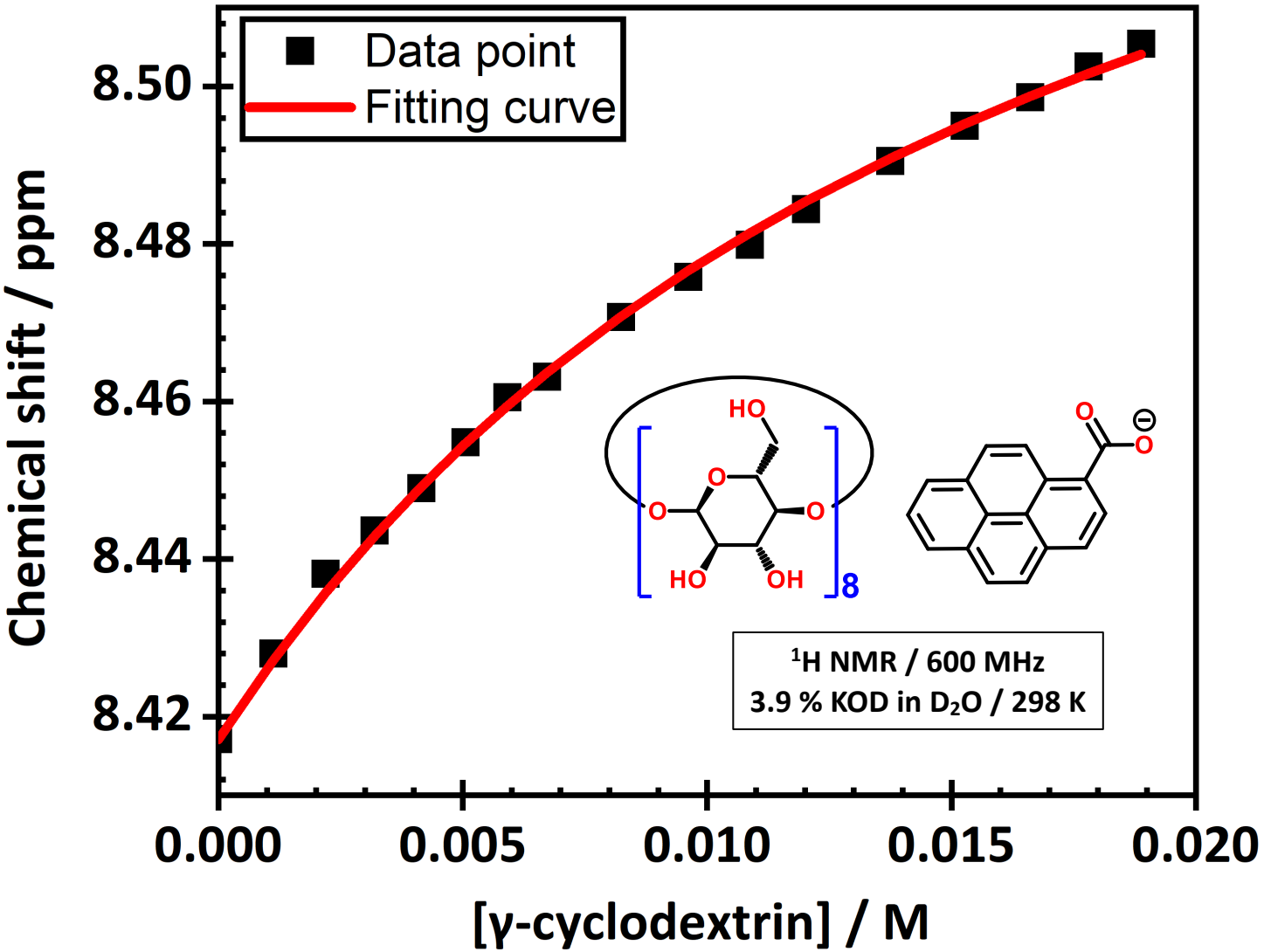

Figure S6. Fitted binding isotherm of PyC^- with γ-CD showing the change in the chemical shift for the ^1H signal at 8.42 ppm upon addition of γ-CD and the fitted isotherm obtained using a 1:1 binding model. $K_a = 62.0 \pm 1.0\ M^{-1}$

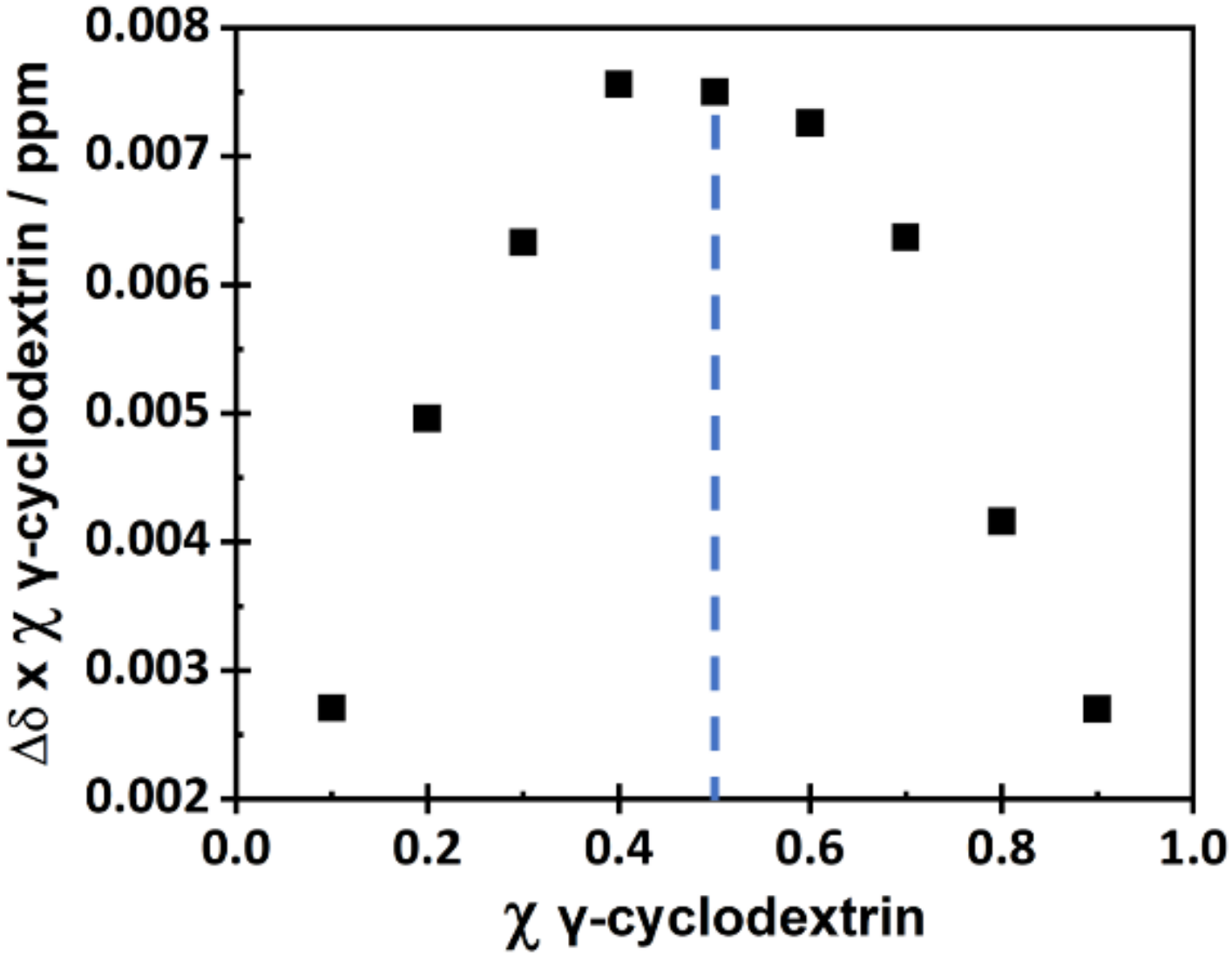

Figure S7. Job plot analysis of the binding ratio γ-CD and PyC^- indicating a 1:1 binding stoichiometry

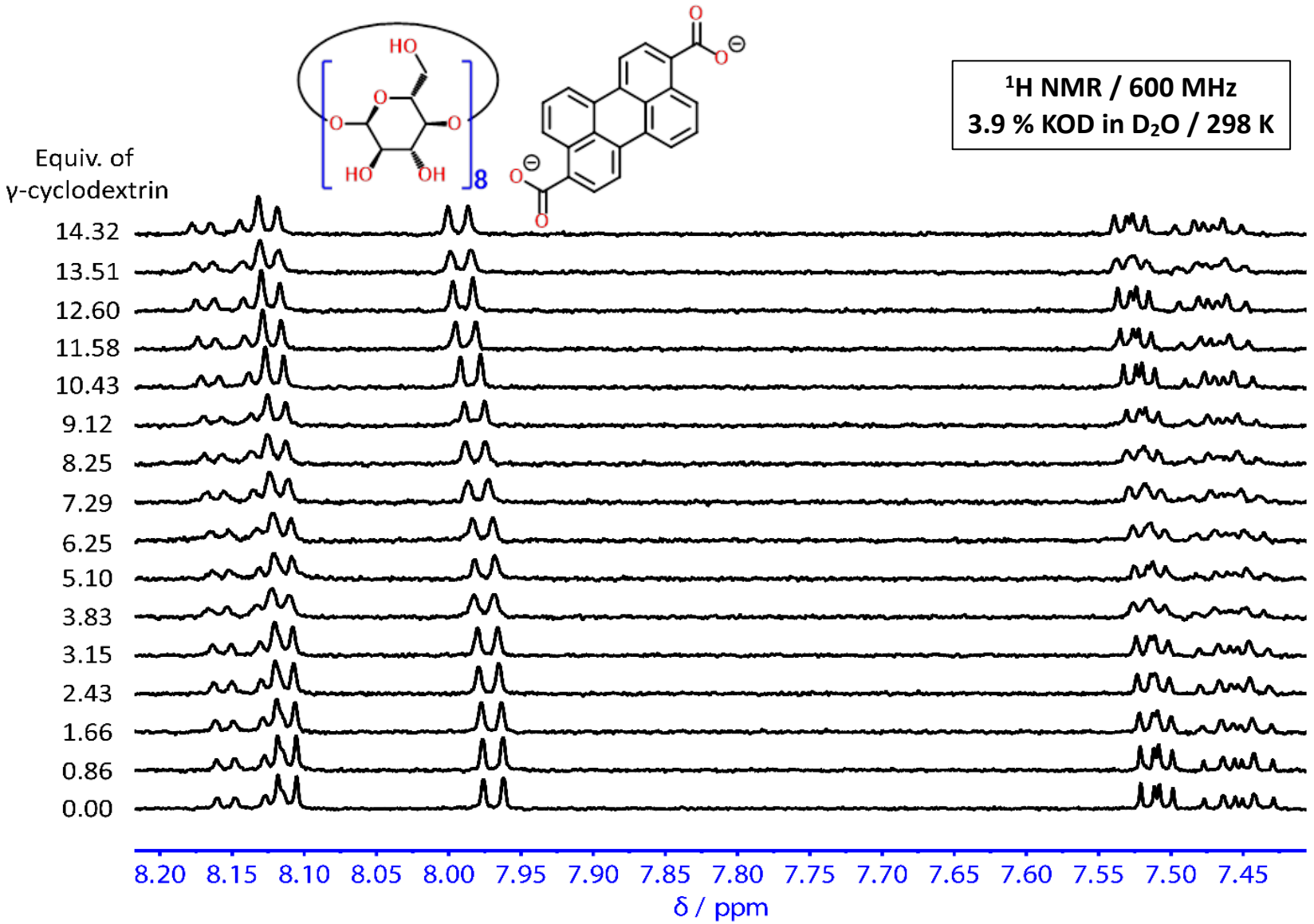

Figure S8. Stacked partial ^{1}H NMR spectra for the titration of PeC^{-} with γ-CD (0 – 14.32 equiv.) displaying minimal changes of chemical shift after the addition of γ-CD

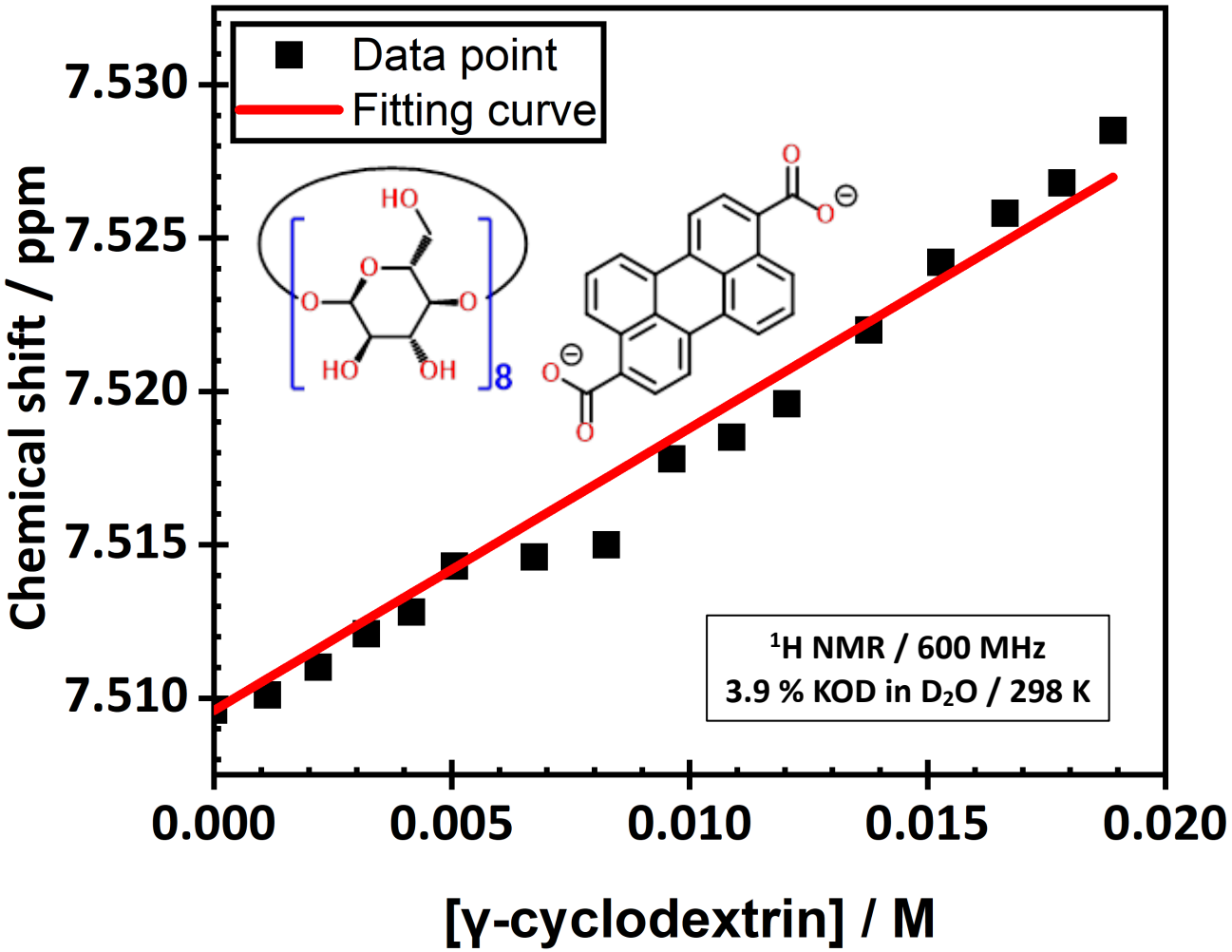

Figure S9. Fitted binding isotherm of PeC^- with γ-CD showing the change in the chemical shift for the ^1H signal at 7.51 ppm upon addition of γ-CD and the fitted isotherm obtained using a 1:1 binding model. K_a = < 0.01 M^{-1}

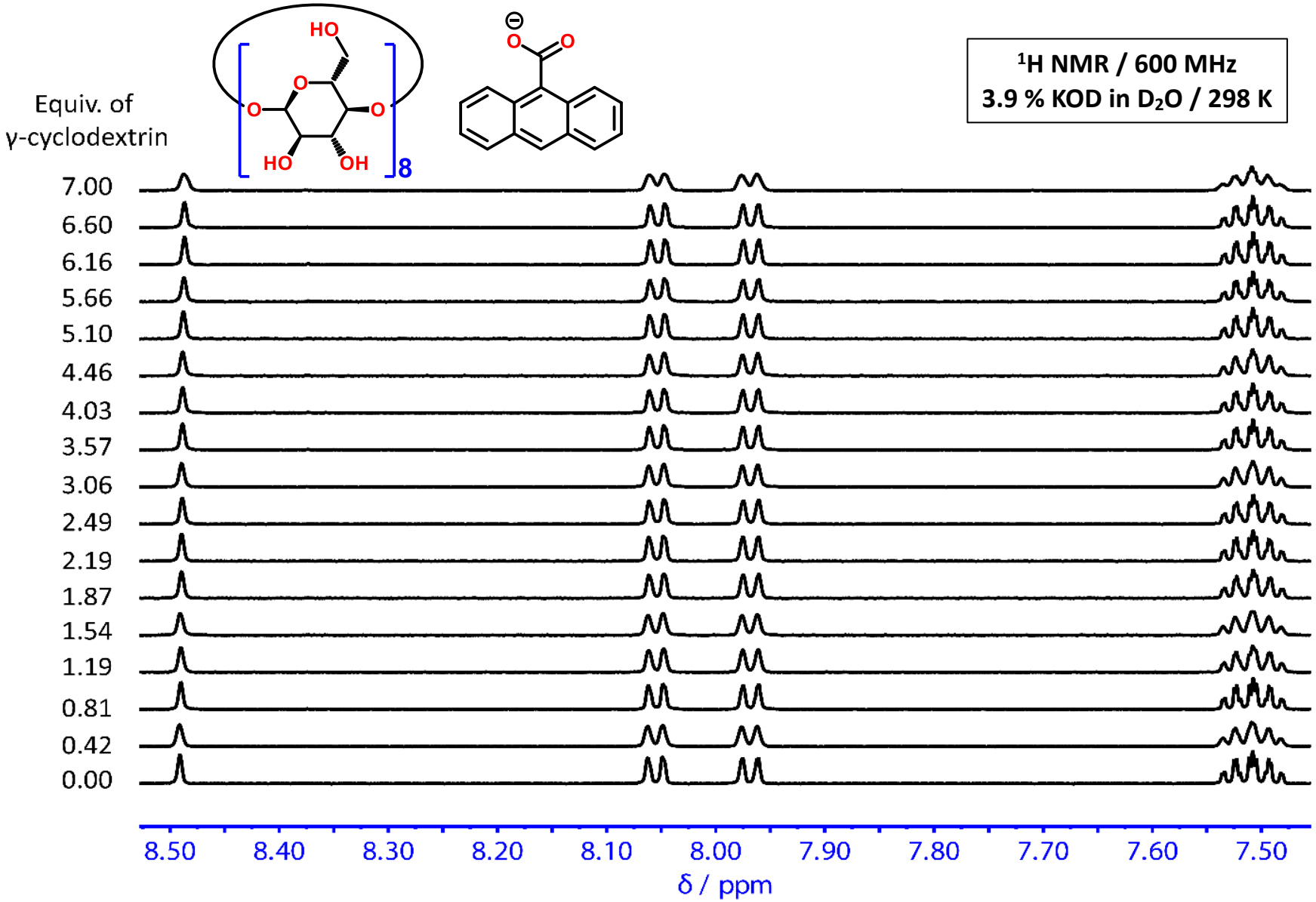

Figure S10. Stacked partial ^{1}H NMR spectra for the titration of AnC^{-} with γ-CD (0 – 7 equiv.) showing no significant change of chemical shift after the addition of γ-CD

Table S3. Titration Details and Calculated Association Constants in Potassium Deuteroxide (3.9%) Solutions in D_2O

Titration Sample	Concentration of carboxylic acid [mM]	Concentration of γ-cyclodextrin [mM]	K_a [M^{-1}]
PyC⁻⊂γ-CD	1.10	38.8	62.0 ± 1.0
AnC⁻⊂γ-CD	2.70	38.8	Negligible
PeC⁻⊂γ-CD	1.32	38.8	Negligible

Section C. Single-Crystal and Powder X-Ray Diffraction

Table S4. Crystal Data and Structure Refinement for $PyC^{-}\subset$CD-HF

Identification code	CCDC-2091539
Empirical formula	$C_{644}H_{1040}K_{24}O_{511}$
Formula weight	17897.10
Temperature / K	100.03(10)
Crystal system	trigonal
Space group	$P3_221$
a / Å, b / Å, c / Å	43.1029(2), 43.1029(2), 56.0818(3)
α/°, β/°, γ/°	90, 90, 120
Volume / $Å^3$	90233.0(10)
Z	3
ρ_{calc} / mg mm^{-3}	0.988
μ / mm^{-1}	1.461
F(000)	28344
Crystal size / mm^3	0.172 × 0.154 × 0.127
2Θ range for data collection	6.46 to 160.642°
Index ranges	$-38 \leq h \leq 53$, $-53 \leq k \leq 39$, $-70 \leq l \leq 68$
Reflections collected	389417
Independent reflections	120924[R(int) = 0.0327]
Data/restraints/parameters	120924/0/5471
Goodness-of-fit on F^2	1.055
Final R indexes [I>2σ (I)]	R_1 = 0.0660, wR_2 = 0.1860
Final R indexes [all data]	R_1 = 0.0740, wR_2 = 0.1974
Largest diff. peak/hole / e $Å^{-3}$	1.268/-0.550

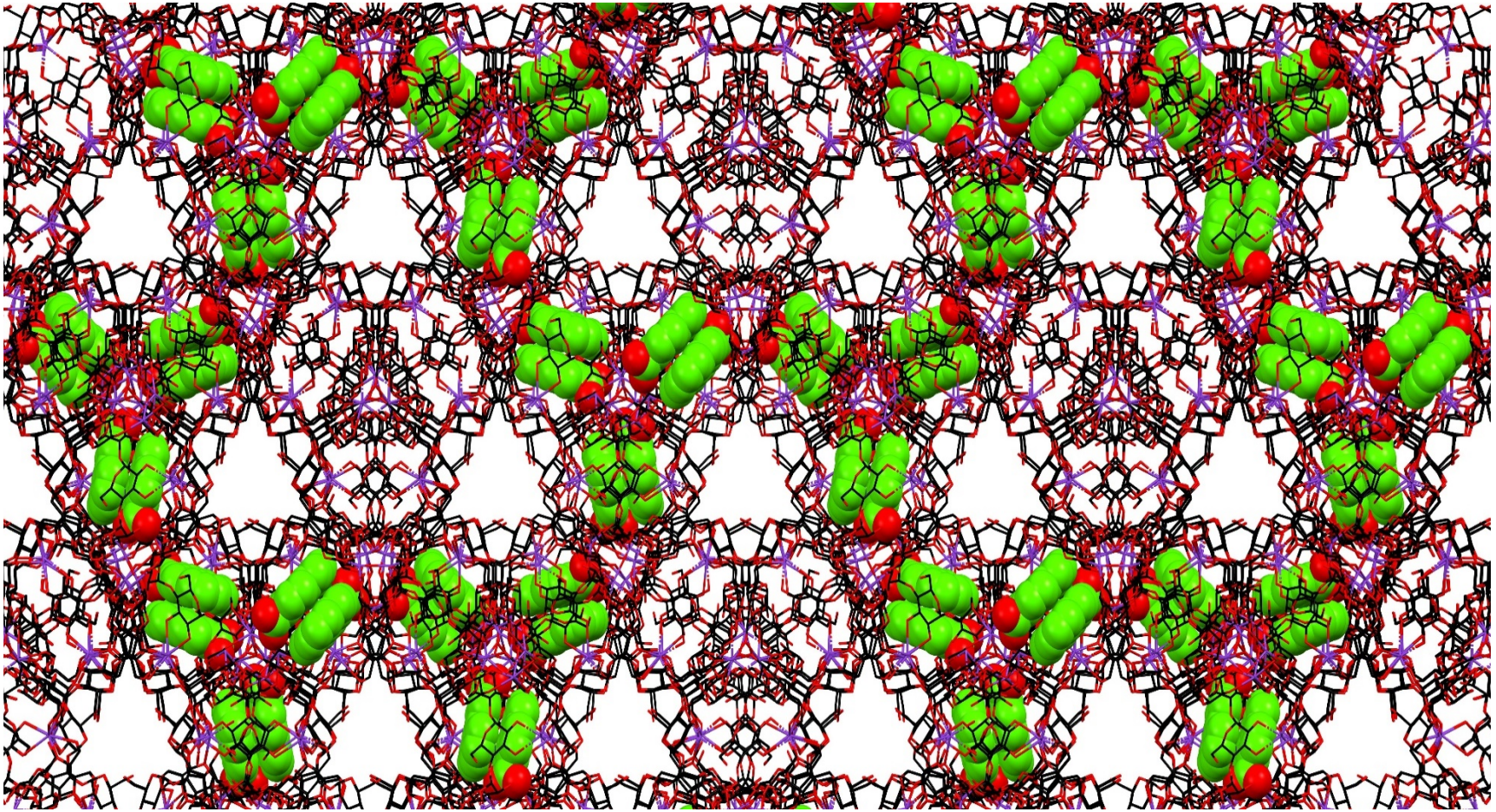

Figure S11. A glimpse of $PyC^{-}\subset$CD-HF superstructure solved by single-crystal X-ray diffraction with a space filling presentation of PyC^{-} in green displaying the MOF in wireframe viewed along *c* cell-axis excluding every proton. CCDC deposition number 2091539, Space Group: $P3_22$ 1, Cell: *a* 43.1 *b* 43.1 *c* 56.0Å, α 90 β 90 γ 120°

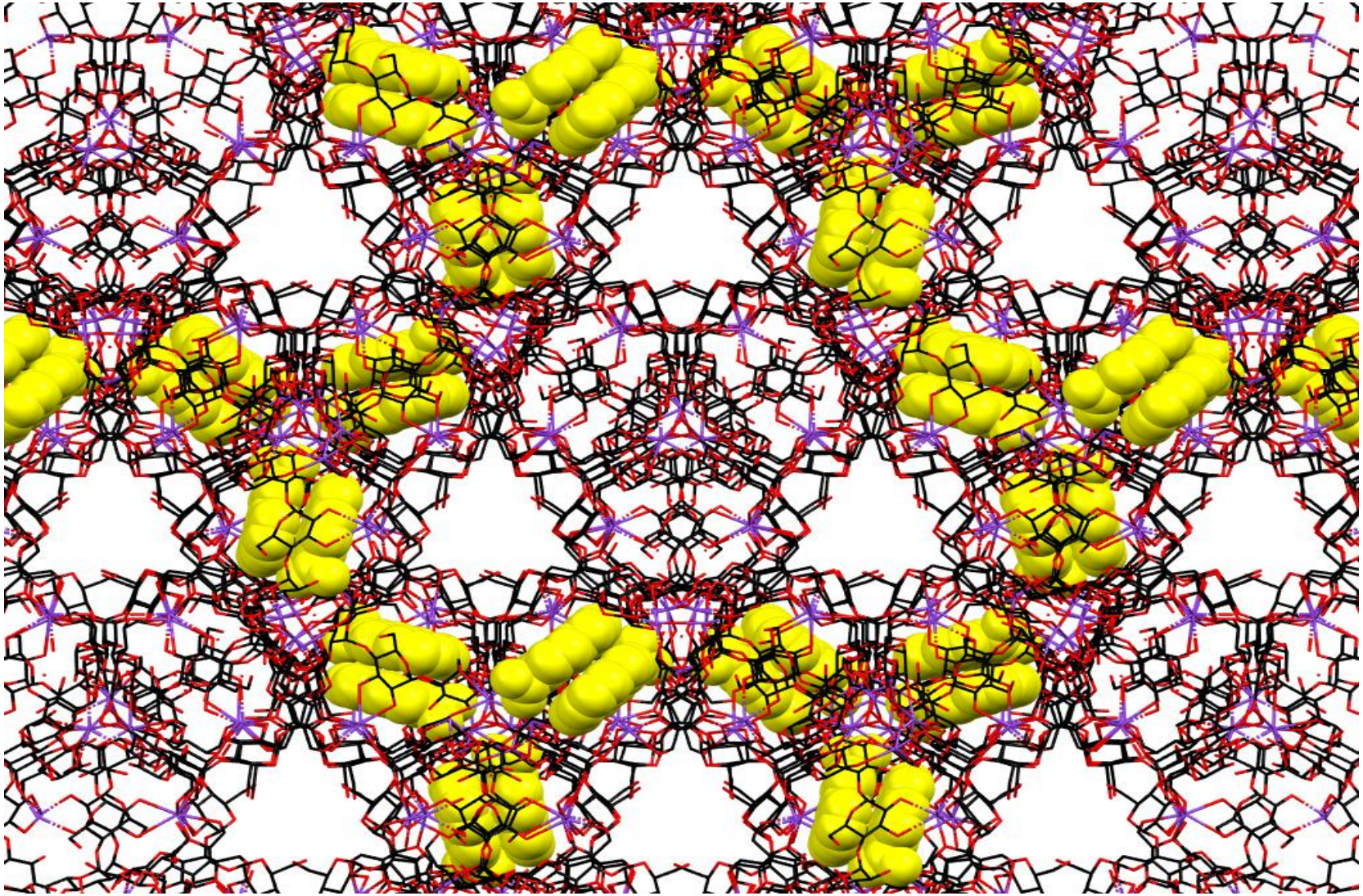

Figure S12. A glimpse of $PyC^{-}\subset$CD-HF superstructure solved by single-crystal X-ray diffraction with a space filling presentation of PyC^{-} in yellow displaying the MOF in wireframe viewed along *c* cell-axis excluding every proton. CCDC deposition number 2091539, Space Group: $P3_22$ 1, Cell: *a* 43.1 *b* 43.1 *c* 56.0Å, α 90 β 90 γ 120°

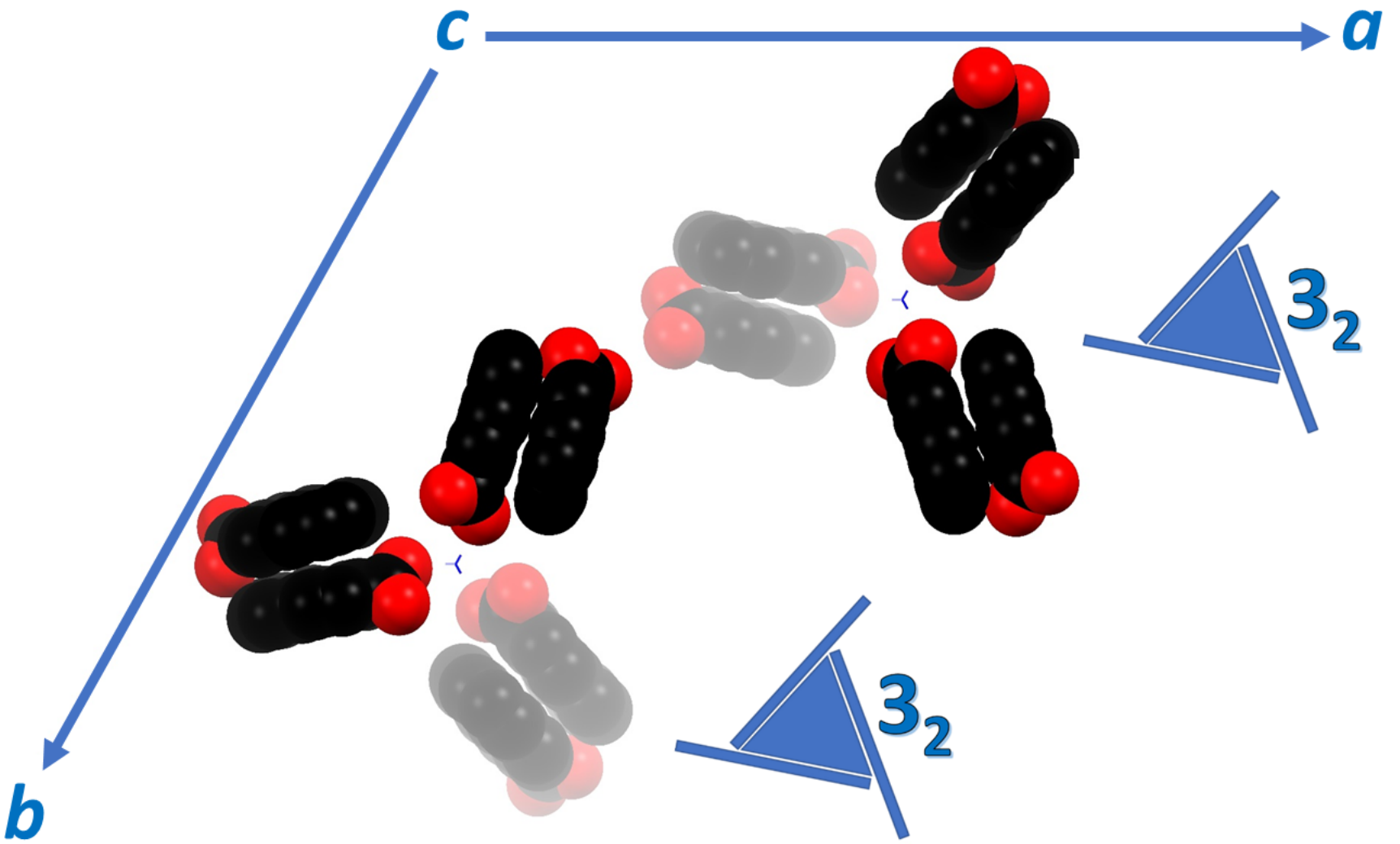

Figure S13. Solid-state superstructure of $PyC^{-}\subset$CD-HF obtained by X-ray diffraction displaying a space filling depth cue presentation of helix-like positioning of the π-stacked PyC^{-} dimers in black around an enantiomorphous 3_2 screw axis viewed along *c* cell-axis while excluding the MOF and every other proton for clarity sake. CCDC deposition number 2091539, Space Group: $P3_22$ 1, Cell: *a* 43.1 *b* 43.1 *c* 56.0Å, *α* 90 *β* 90 *γ* 120°

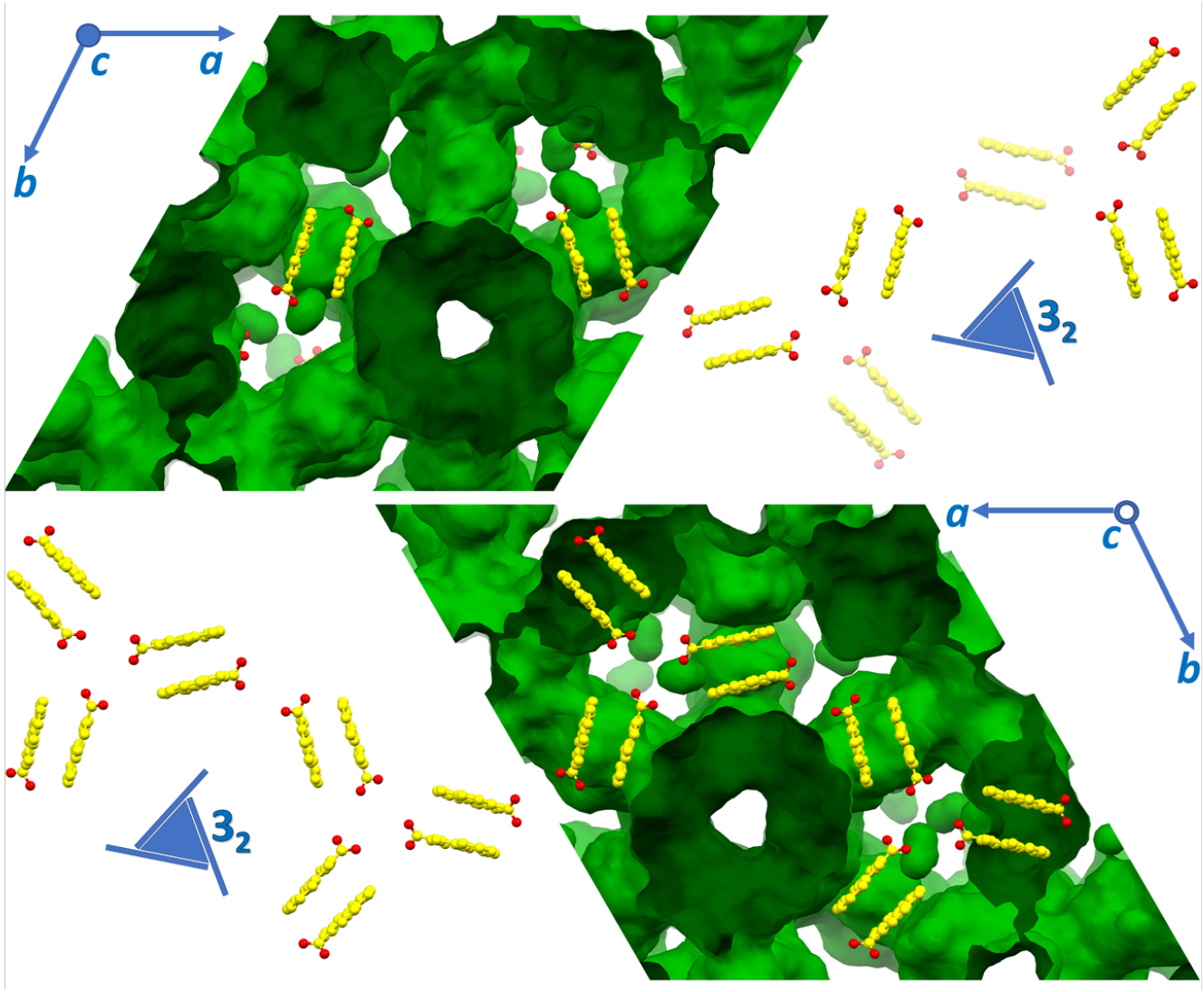

Figure S14. Helix-like positioning of π-stacked PyC^{-} with and without the color-coded presentation of the chiral voids of the unit cell viewed along *c* cell-axis (top row) and c^{*} cell-axis (bottom row).
CCDC deposition number 2091539, Space Group: $P3_22$ 1, Cell: *a* 43.1 *b* 43.1 *c* 56.0Å, α 90 β 90 γ 120°

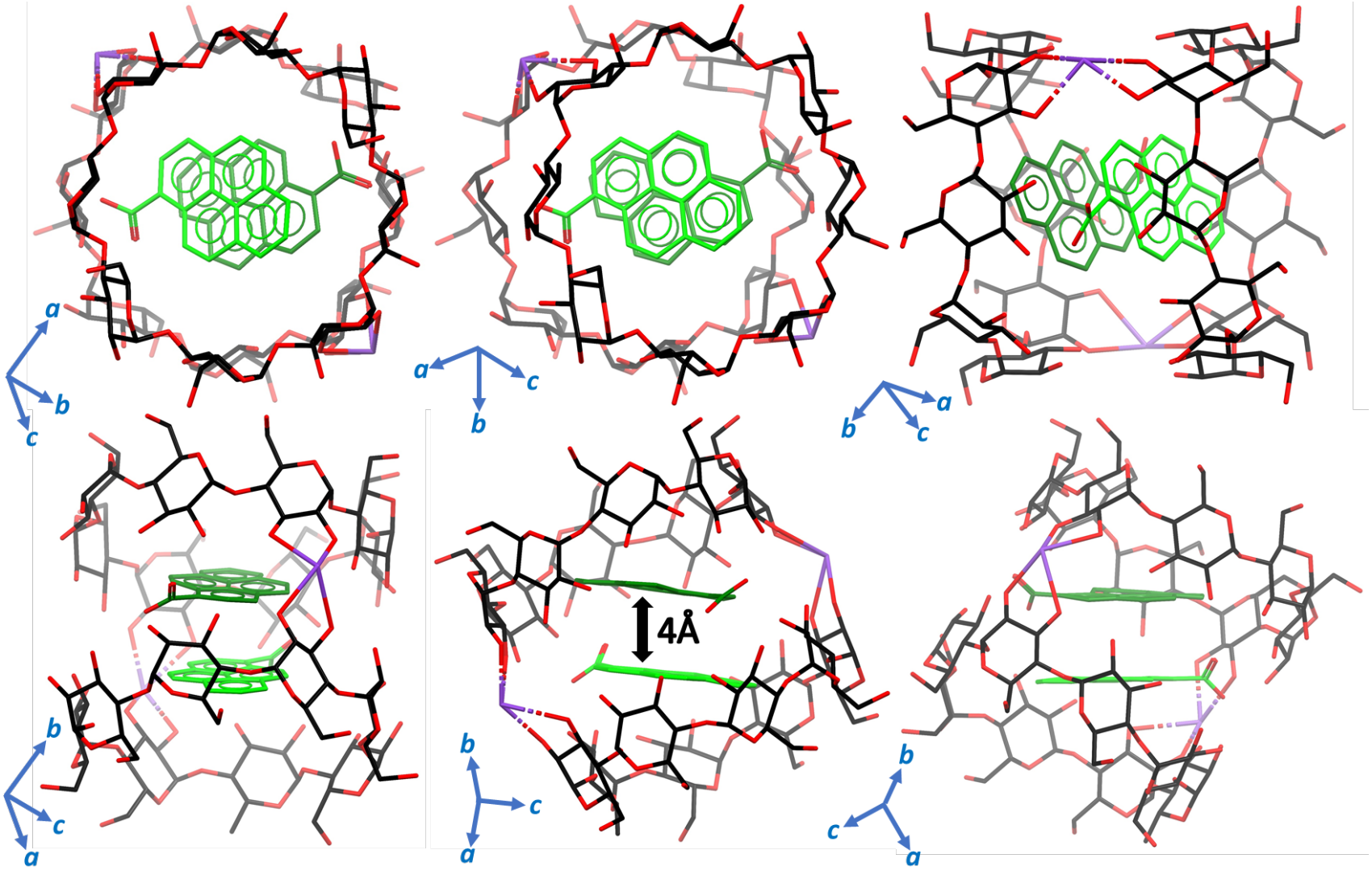

Figure S15. Side-views of (γ-CD)$_2$ tunnel obtained by solid-state X-ray diffraction tilted at various angels displaying unit cell axis in blue and excluding the protons and neighboring molecules.
CCDC deposition number 2091539, Space Group: $P3_22$ 1, Cell: a 43.1 b 43.1 c 56.0Å, α 90 β 90 γ 120°

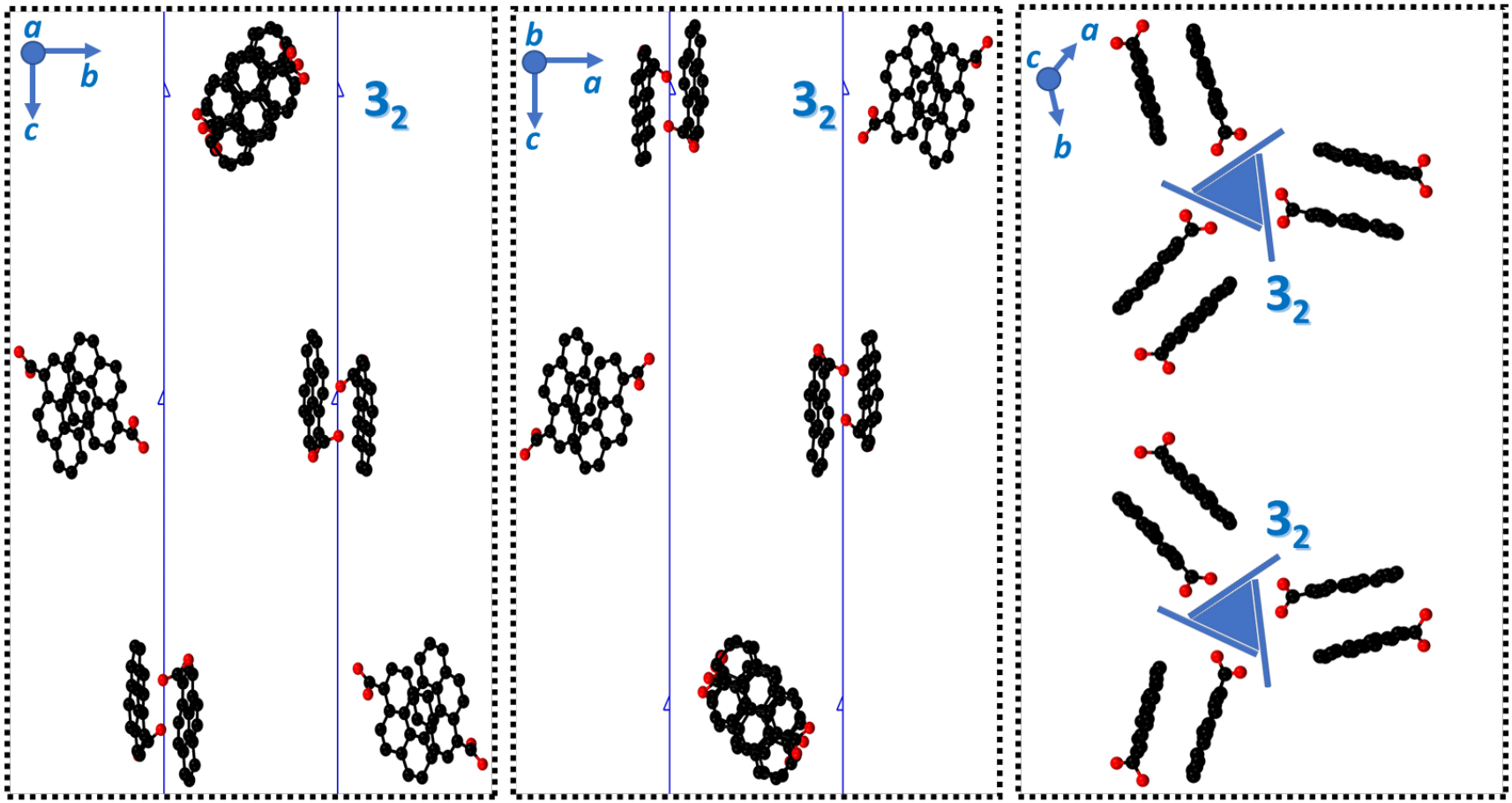

Figure S16. Solid-state superstructure of $PyC^{-}\subset$CD-HF displaying the chiral helix-like positioning of the π-stacked PyC^{-} molecules held around enantiomorphous 3_2 screw axis (shown in blue) viewed along *a*-axis (left), *b*-axis (middle), and *c*-axis (right) excluding the MOF and every proton for clarity.
CCDC deposition number 2091539, Space Group: $P3_22\ 1$, Cell: *a* 43.1 *b* 43.1 *c* 56.0Å, α 90 β 90 γ 120°

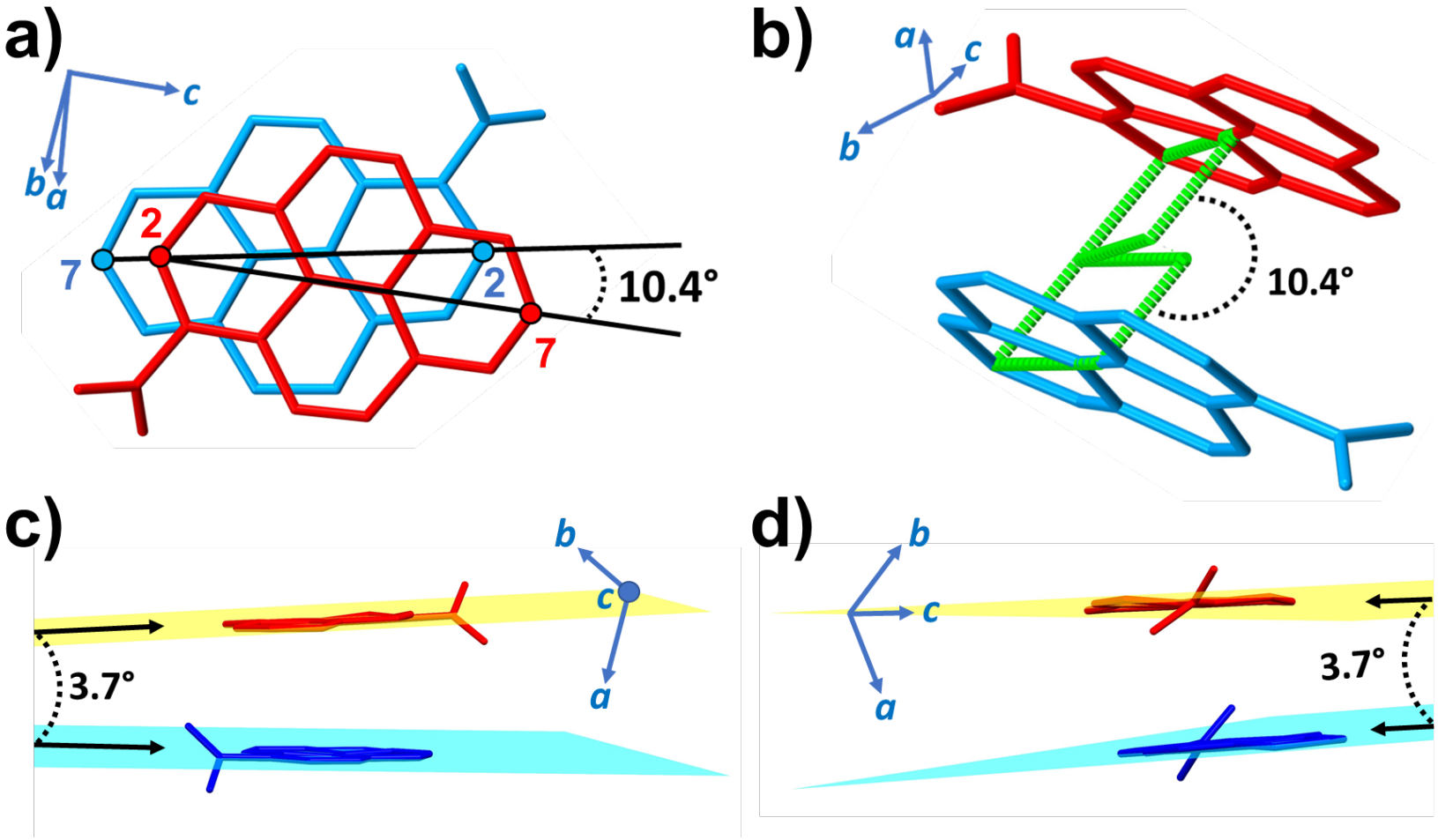

Figure S17. X-Ray diffraction data showing the relative orientation of pyrene units in $PyC^{-}\subset$CD-HF. (a, b) Two views of the 10.4° angle depicting the relative rotation of the π-stacked PyC^{-} units, taking carbons 2 and 7 of each pyrene as reference points (colored dots). (c, d) Two views of the 3.7° angle existing between the aromatic planes of a single π-stacked PyC^{-} dimer, where all 17 carbons of the blue PyC^{-} molecule lie in the cyan plane, and all 17 carbons of the red PyC^{-} molecule lie in the yellow plane. Blue arrows indicate the direction of the unit cell axis. CCDC Deposition number 2091539, Space Group: $P3_22$ 1, Cell: a 43.1 b 43.1 c 56.0Å, α 90 β 90 γ 120°

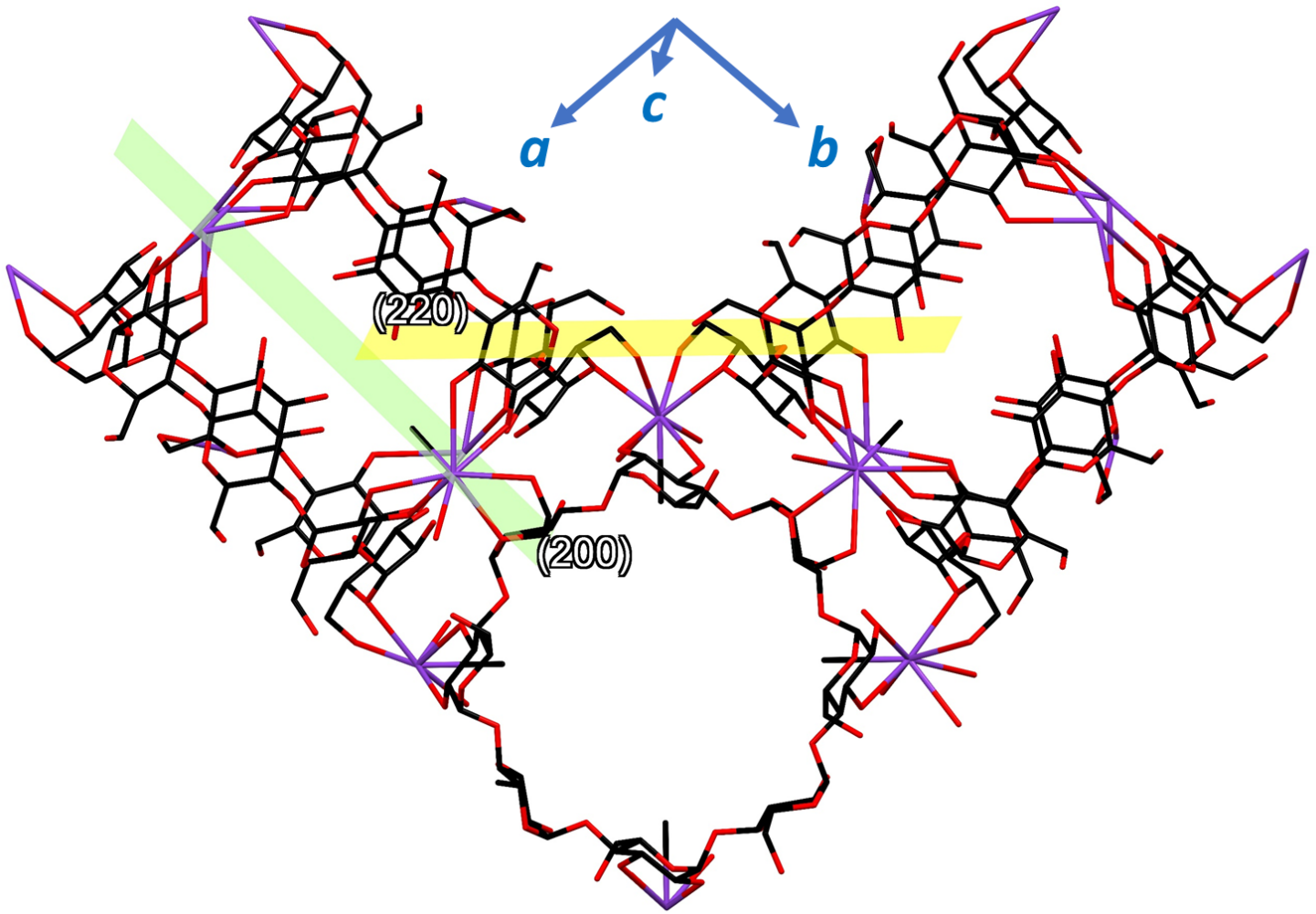

Figure S18. Solid-state superstructure of CD-MOF-1 obtained by X-ray diffraction, indicating the location of planes with {*hkl*} integers equivalent to Miller indices (200) and (220) shown in light green and yellow respectively, that correspond to the specific angles of 5.7° and 8.0° at which PXRD pattern of AnC^{-}⊂CD-MOF-1 shows suppression of peak intensities compared to those of pristine CD-MOF-1.

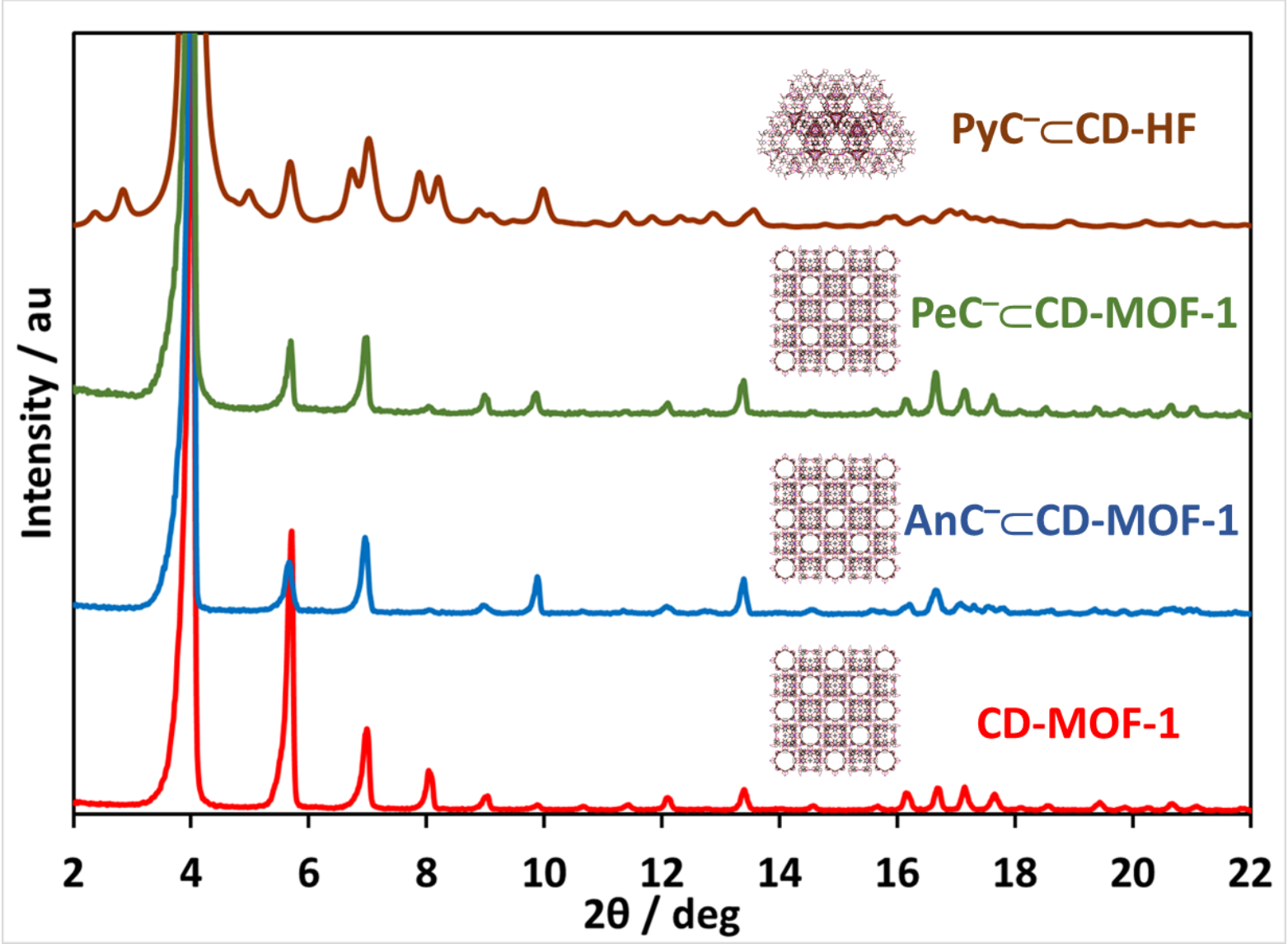

Figure S19. Comparative X-ray powder diffraction patterns of pristine CD-MOF-1 and dye-loaded ones

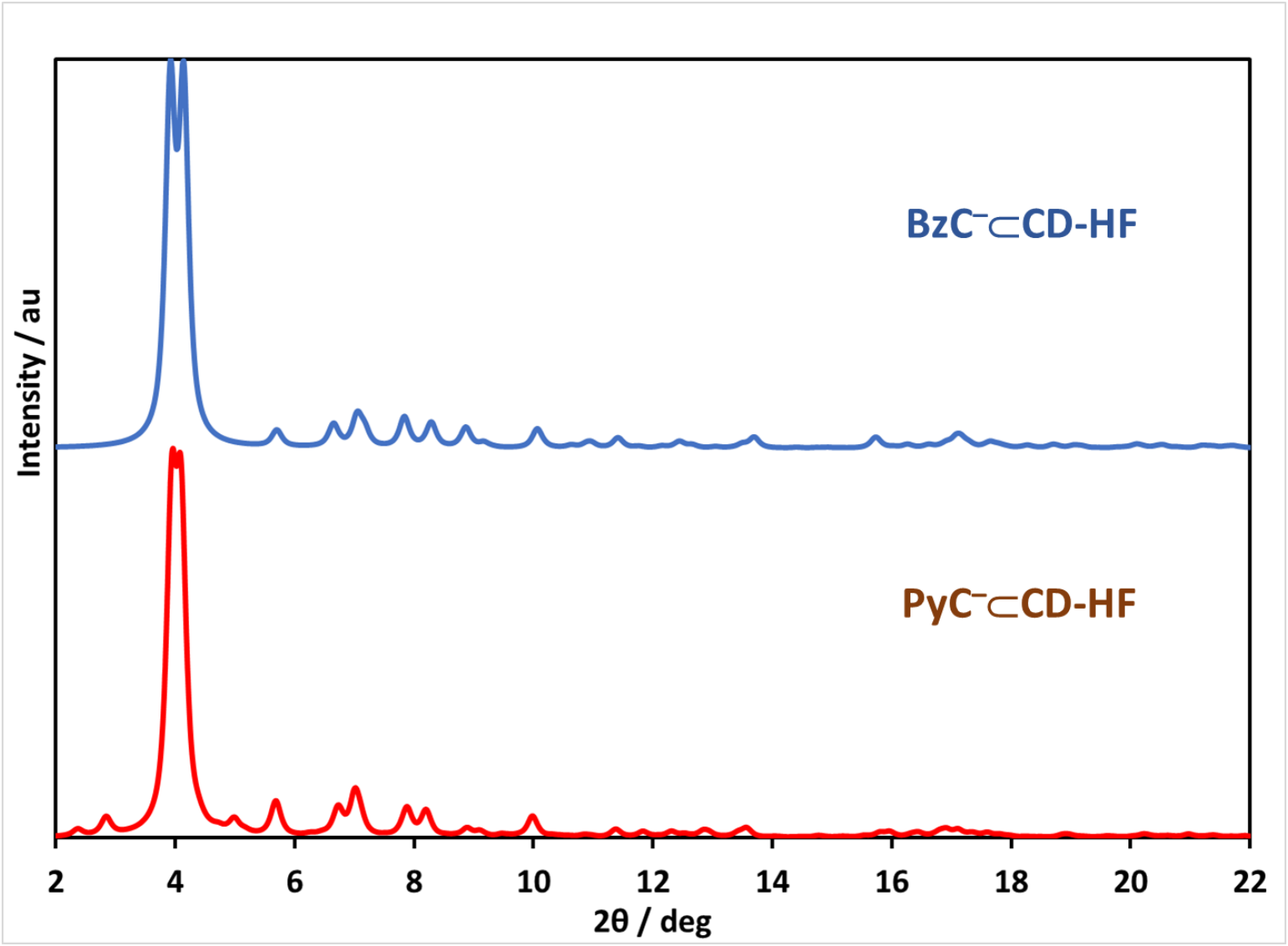

Figure S20. PXRDs obtained from PyC⁻⊂CD-HF, and simulated for benzoic acid carrying MOF (BzC⁻⊂CD-HF)[S1]

Section D. Fluorescence and Scanning Electron Microscopy Imaging

Figure S21. Photograph of vials illuminated at 365 nm containing $PyC^{-}\subset$CD-HF kept in the mother liquor (left), and fresh MeOH (right)

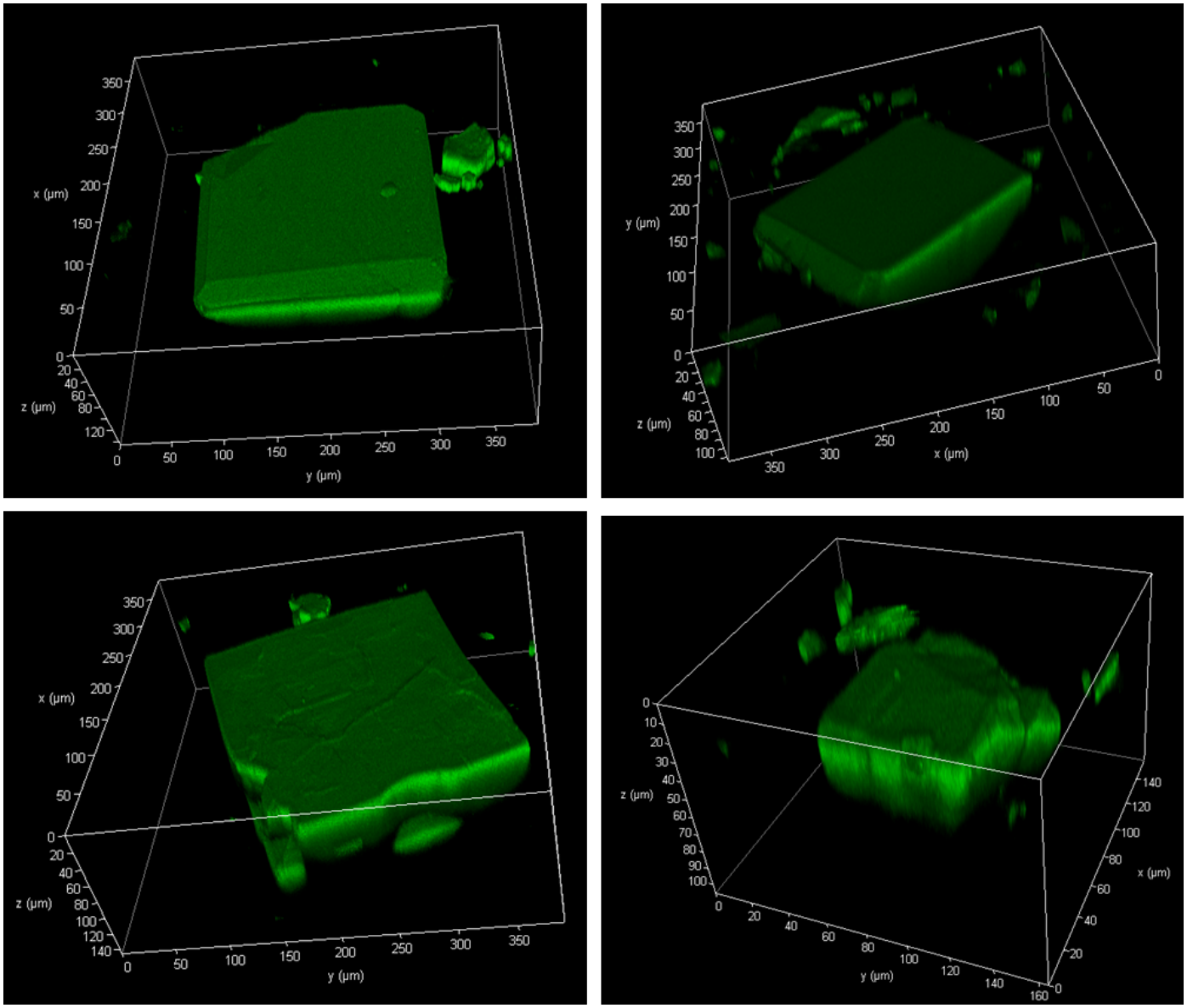

Figure S22. Fluorescence microscope imaging of $PyC^{-}\subset$CD-HF illuminated at 365 nm

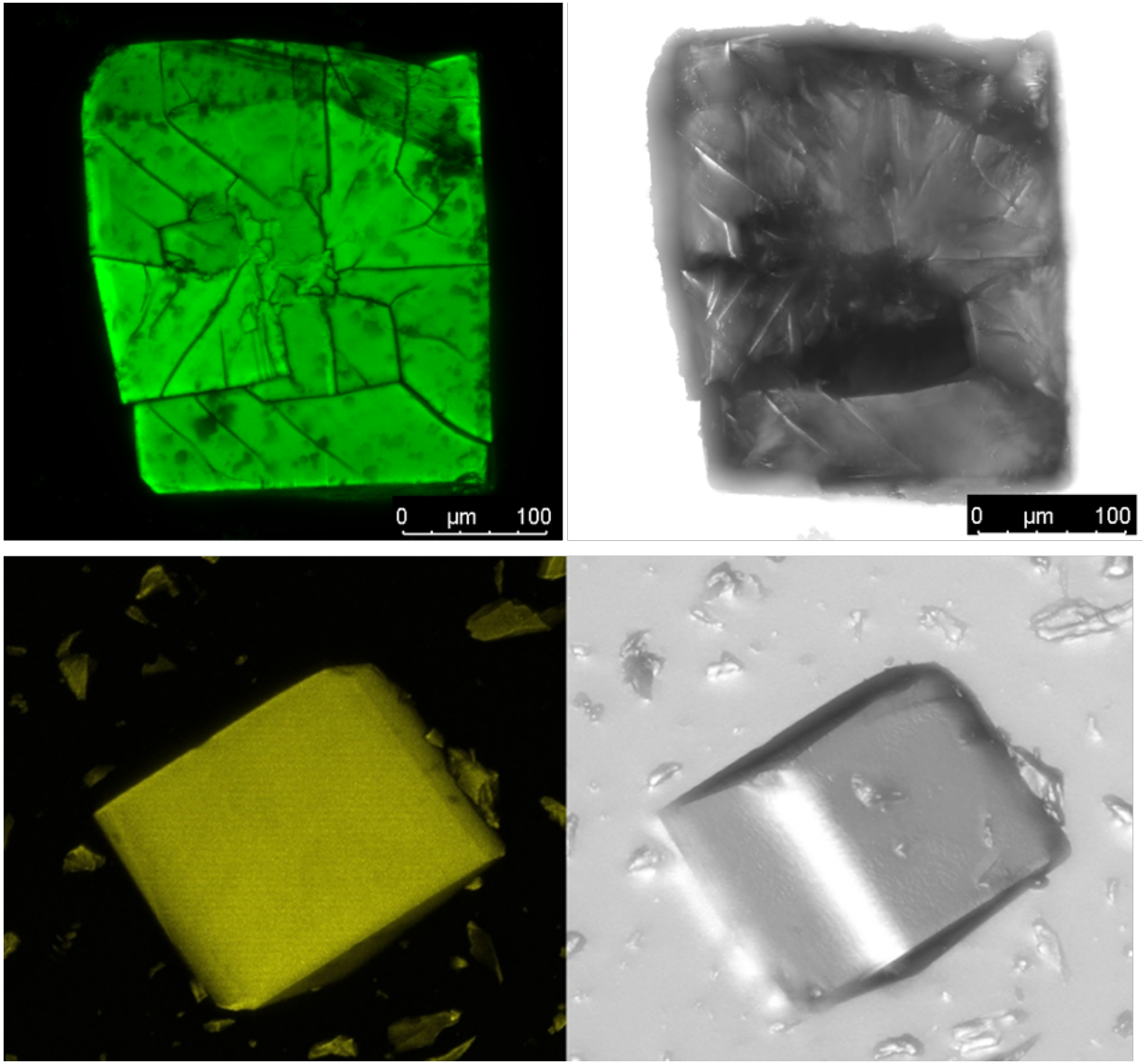

Figure S23. Fluorescence microscope imaging of $PyC^{-}\subset$CD-HF illuminated at 365 nm

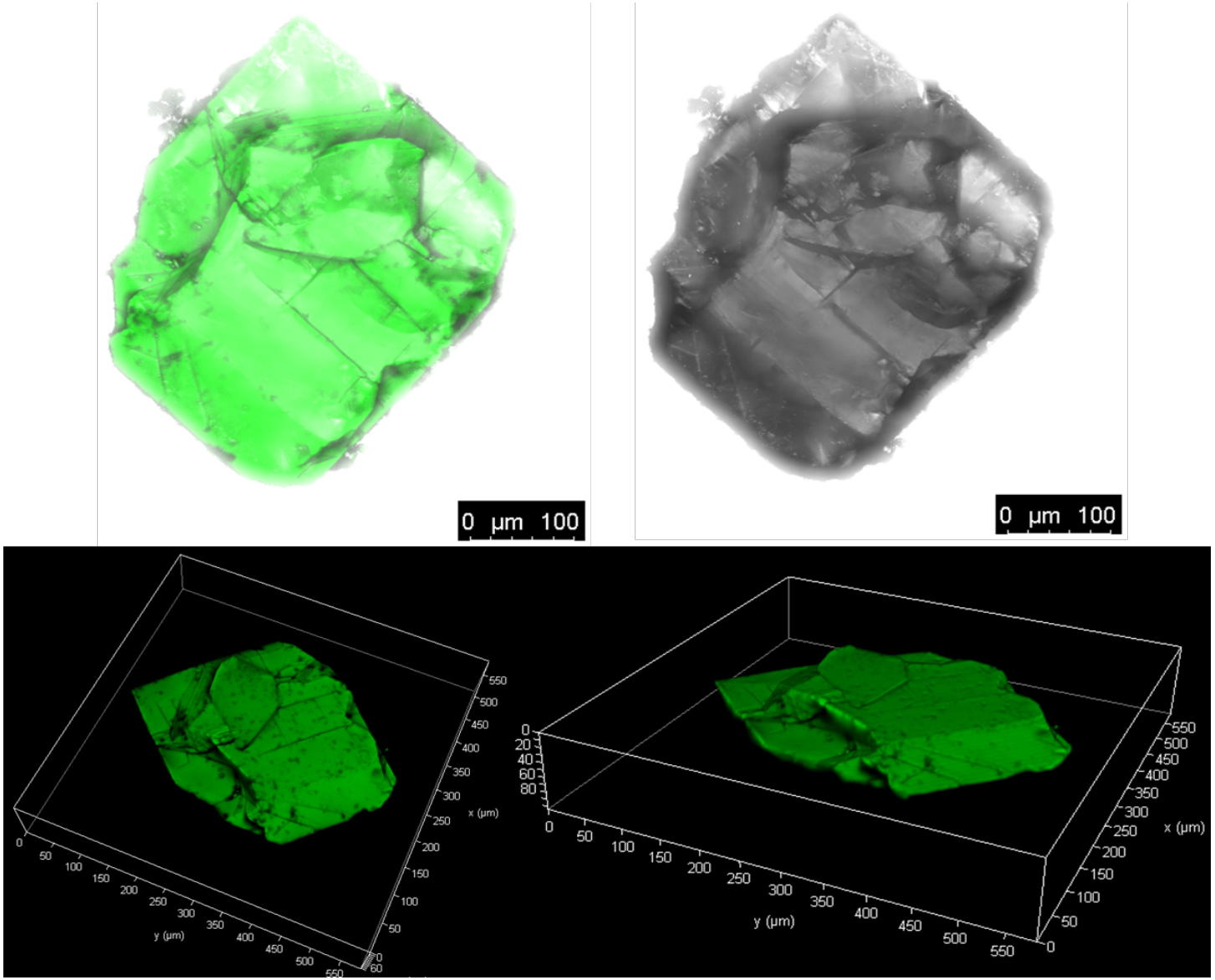

Figure S24. Fluorescence microscope imaging of $PyC^{-}\subset$CD-HF illuminated at 365 nm

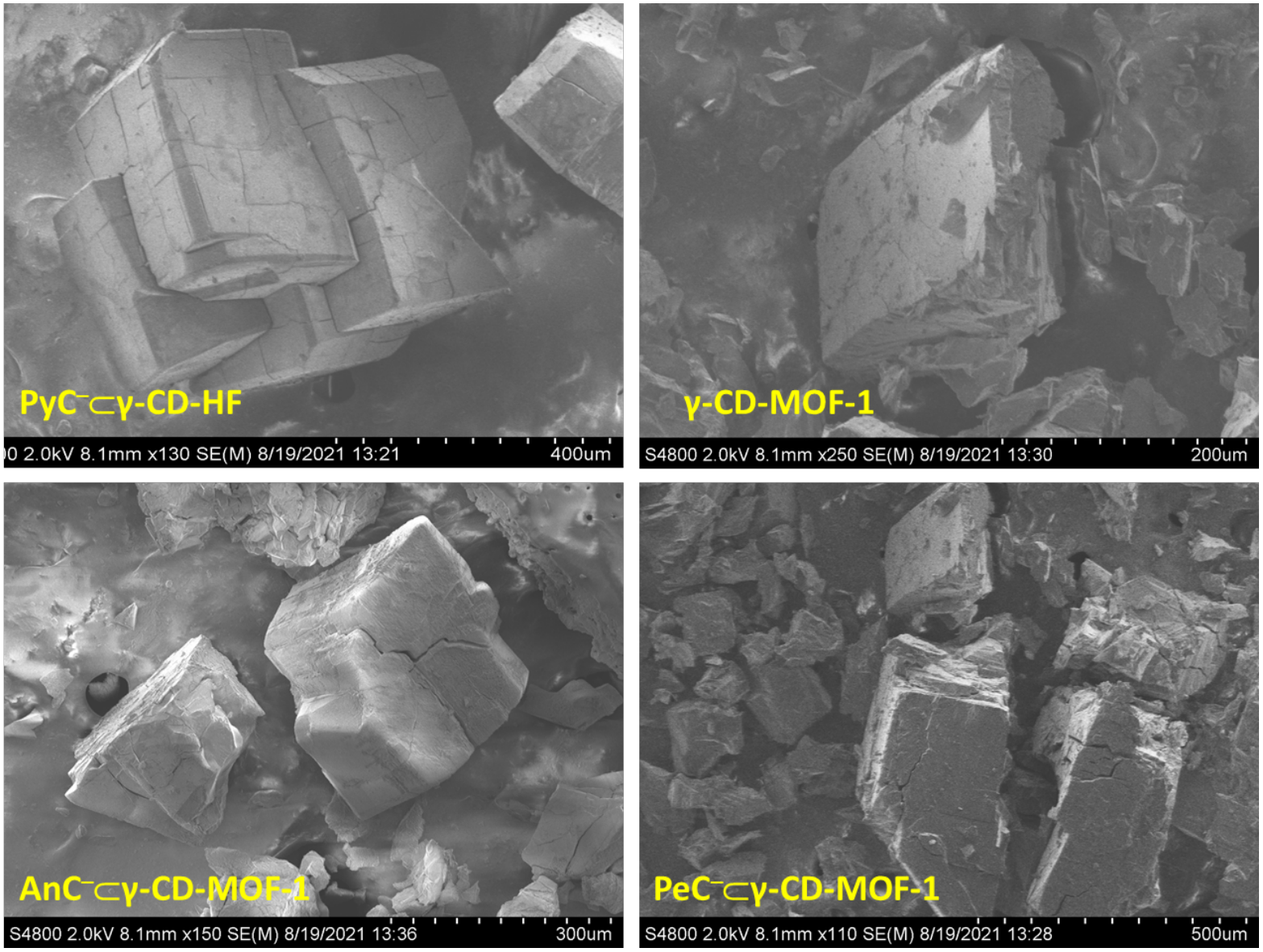

Figure S25. Scanning electron microscope imaging of the CD-MOFs

Section E. Steady-State and Time-Resolved Fluorescence Spectroscopy

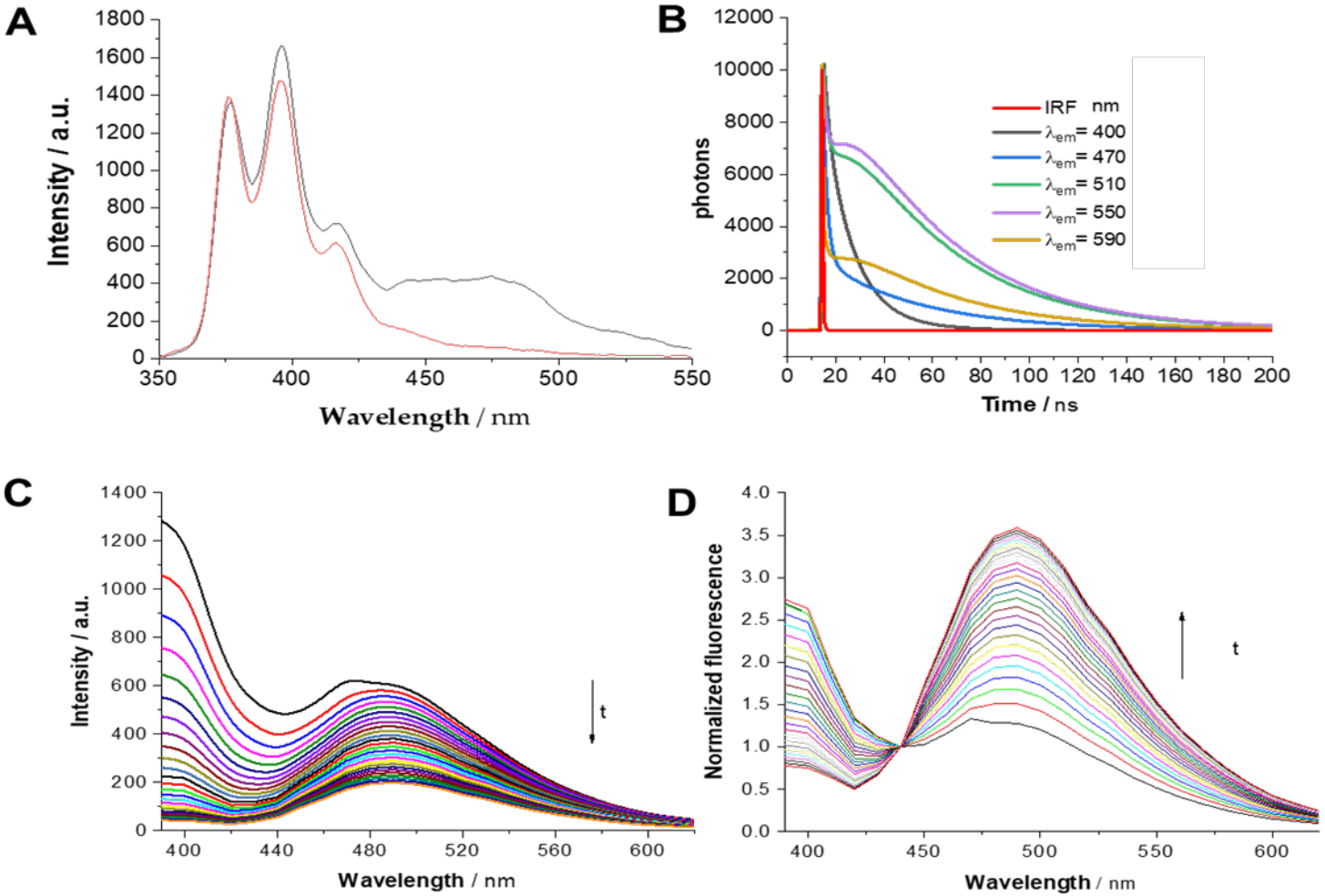

Figure S26. A) Emission spectra (λ_{exc}= 300nm) of of $PyC^{-}\subset$CD-HF crystals suspended in MeOH (black line) and decanted solution formed after time (red line). B) Luminescence decay traces of $PyC^{-}\subset$CD-HF crystals suspended in MeOH (λ_{ex} = 375 nm) collected at the λ_{em} of 400 (grey), 470 (blue), 510 (green), 550 (violet) and 590 nm (dark yellow). The instrument response function (IRF) of the laser source is also shown in red. C) Evolution of emission spectra of $PyC^{-}\subset$CD-HF crystals suspended in MeOH at differ[illegible]mes after a δ-pulse excitation, from 0 to 50 ns after the excitation pulse. D) Evolution of normalized (at 440nm) emission spectra from panel B of $PyC^{-}\subset$CD-HF crystals suspended in MeOH.

Section F. Fluorescence Lifetime Imaging Microscopy (FLIM)

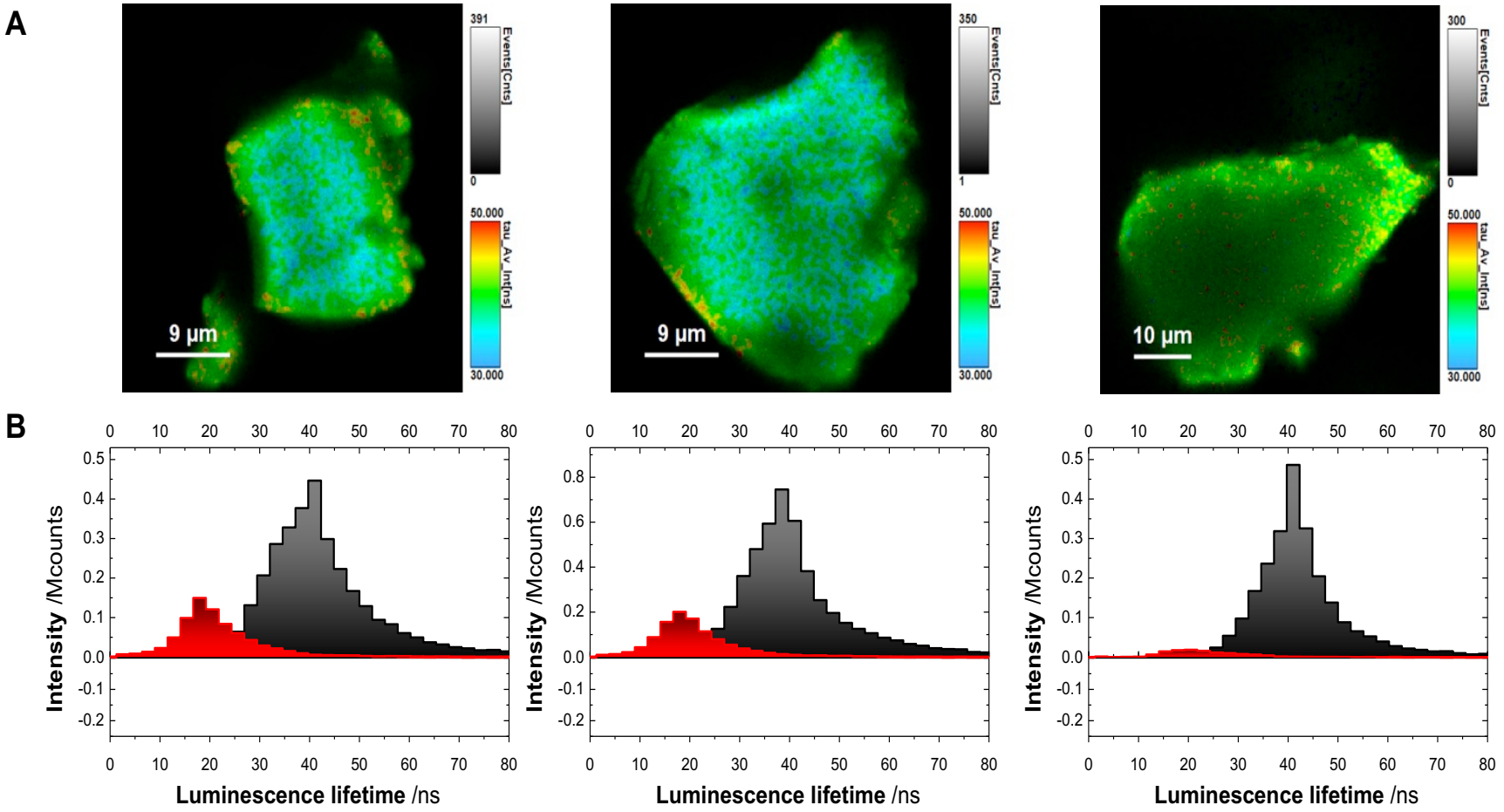

Figure S27. A) FLIM images (λ_{ex} = 375 nm) of individual $PyC^{-}\subset$CD-HF crystals in solid-state. B) The corresponding luminescence lifetime distributions extracted from the images

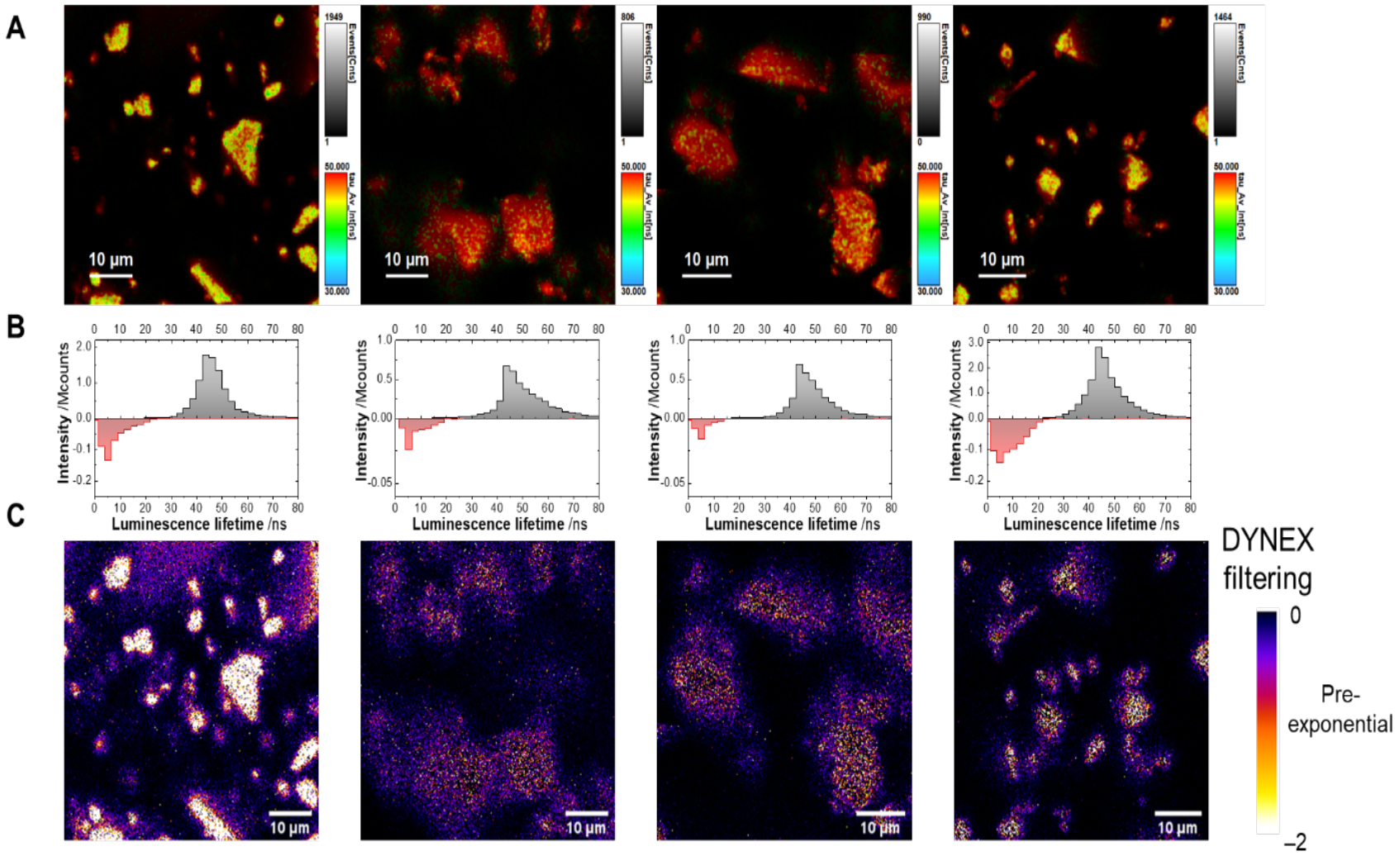

Figure S28. A) FLIM images of $PyC^{-}\subset$CD-HF crystals suspended in MeOH (λ_{ex} = 375 nm) and the corresponding. B) luminescence lifetime distributions extracted from the images and C) DYNEX filtering analysis.

Section G. Theoretical Calculations

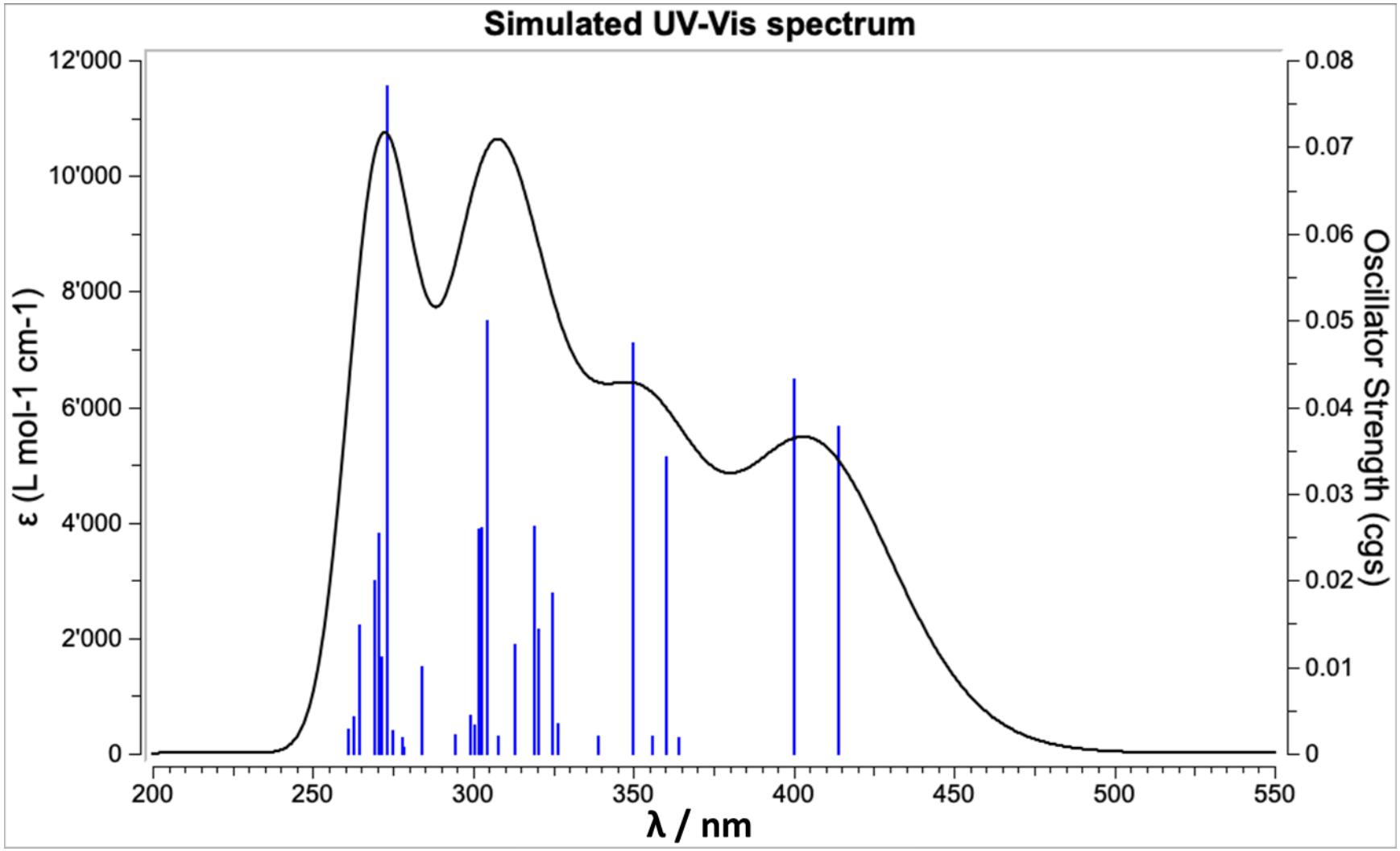

Figure S29. Calculated electronic transitions and simulated UV-Vis spectrum of the PyC^{-}–PyC^{-}

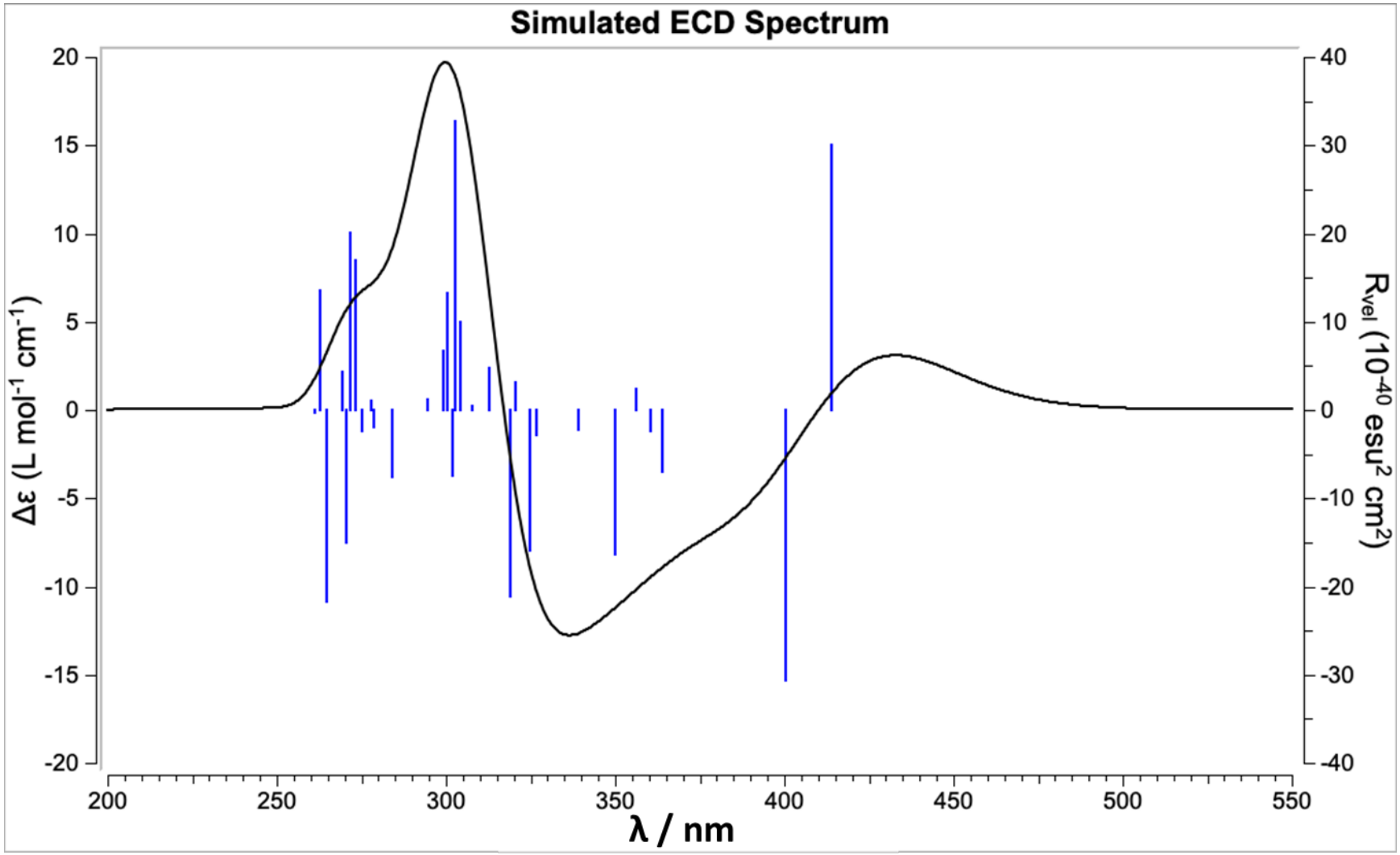

Figure S30. Calculated rotatory strengths and simulated ECD spectrum of the PyC^{-}–PyC^{-}

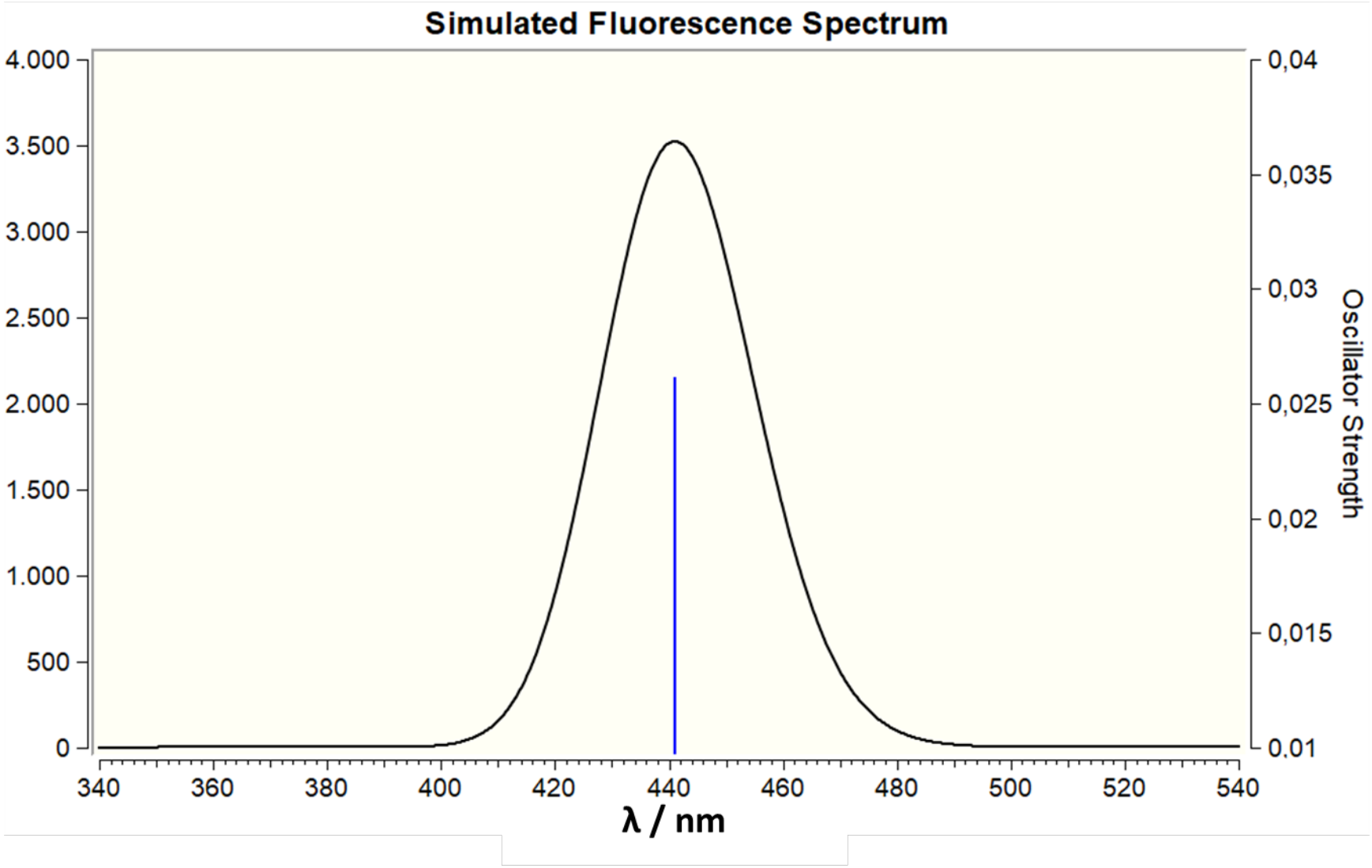

Figure S31. Calculated $S_1 \rightarrow S_0$ transition and simulated fluorescence spectrum of the PyC^{-}–PyC^{-}

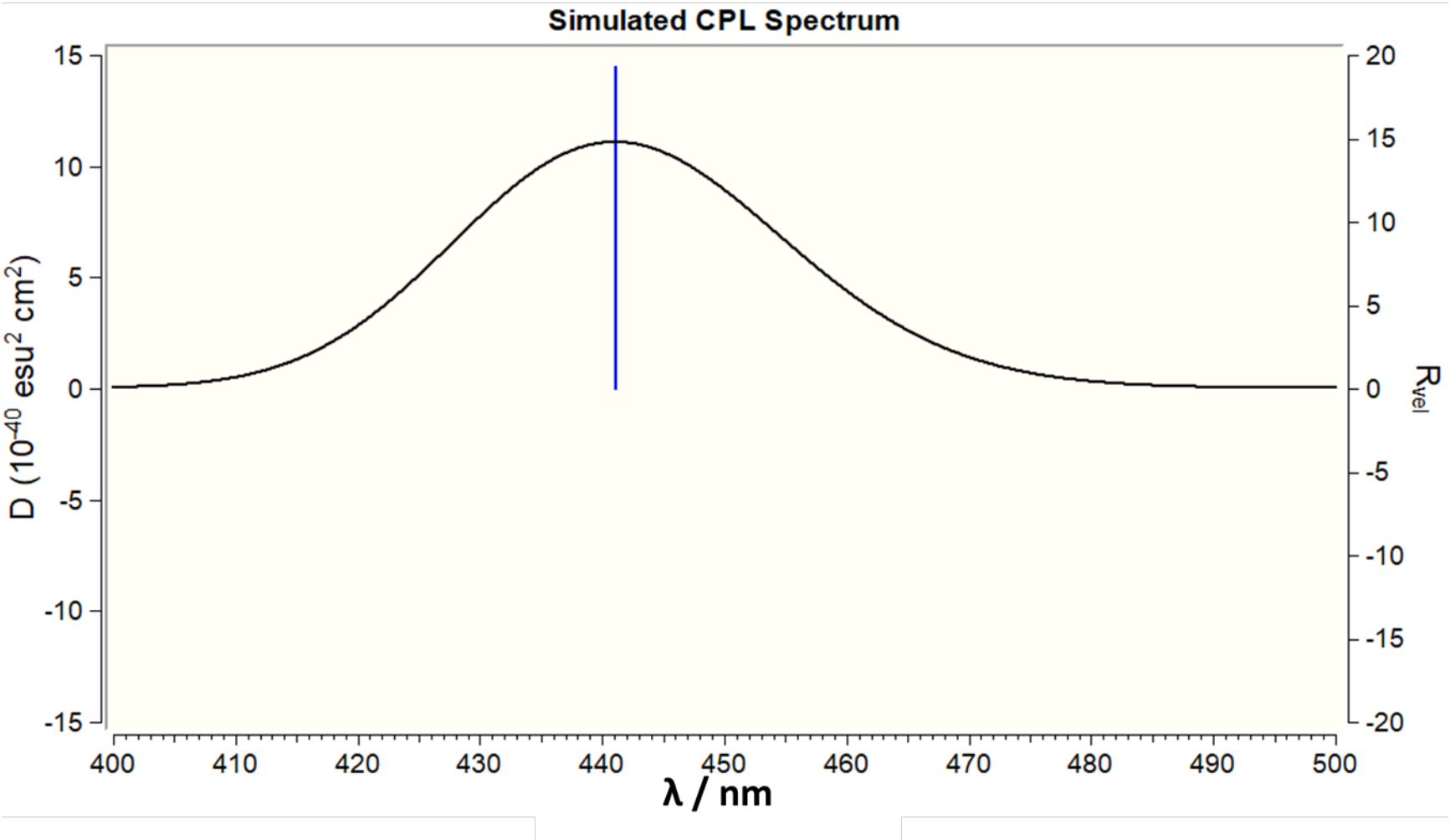

Figure S32. Calculated rotatory strength and simulated CPL spectrum of the PyC^{-}–PyC^{-}

References

(S1) Smaldone, R. A.; Forgan, R. S.; Furukawa, H.; Gassensmith, J. J.; Slawin, A. M. Z.; Yaghi, O. M.; Stoddart, J. F., Metal–Organic Frameworks from Edible Natural Products. *Angew. Chem. Int. Ed.* **2010**, *49*, 8630–8634.

(S2) (a) Hartlieb, K. J.; Ferris, D. P.; Holcroft, J. M.; Kandela, I.; Stern, C. L.; Nassar, M. S.; Botros, Y. Y.; Stoddart, J. F., Encapsulation of Ibuprofen in CD-MOF and Related Bioavailability Studies. *Mol. Pharmaceutics* **2017**, *14*, 1831–1839. (b) Chen, X.-Y.; Chen, H.; Đorđević, L.; Guo, Q.-H.; Wu, H.; Wang, Y.; Zhang, L.; Jiao, Y.; Cai, K.; Chen, H.; Stern, C. L.; Stupp, S. I.; Snurr, R. Q.; Shen, D.; Stoddart, J. F., Selective Photodimerization in a Cyclodextrin Metal–Organic Framework. *J. Am. Chem. Soc.* **2021**, *143*, 9129–9139.

(S3) Dolomanov, O.V.; Bourhis, L. J.; Gildea, R. J.; Howard, J. A. K.; Puschmann, H., *OLEX2*: A Complete Structure Solution, Refinement and Analysis Program. *J. Appl. Cryst.* **2009**, *42*, 339–341.

(S4) Sheldrick, G.M., *SHELXT* - Integrated Space-Group and Crystal-Structure Determination. *Acta Cryst.* **2015**, *A71*, 3–8.

(S5) Sheldrick, G.M., A Short History of SHELX. *Acta Cryst.* **2008**, *A64*, 112–122.

(S6) Thordarson, P., Determining Association Constants from Titration Experiments in Supramolecular Chemistry. *Chem. Soc. Rev.* **2011**, *40*, 1305–1323.

(S7) Gonzalez-Garcia, M. C.; Salto-Giron, C.; Herrero-Foncubierta, P.; Peña-Ruiz, T.; Giron-Gonzalez, M. D.; Salto-Gonzalez, R.; Perez-Lara, A.; Navarro, A.; Garcia-Fernandez, E.; Orte, A., Dynamic Excimer (Dynex) Imaging of Lipid Droplets. *ACS Sensors* **2021**, *6*, 3632–3639.

(S8) Blok, P. M. L.; Dekkers, H. P. J. M., Measurement of the Circular Polarization of the Luminescence of Photoselected Samples under Artifact-Free Conditions. *Appl. Spectrosc.* **1990**, *44*, 305–309.

(S9) Amako, T.; Nakabayashi, K.; Suzuki, N.; Guo, S.; Rahim, N. A. A.; Harada, T.; Fujiki, M.; Imai, Y., Pyrene Magic: Chiroptical Enciphering and Deciphering 1,3-Dioxolane Bearing Two Wirepullings to Drive Two Remote Pyrenes. *Chem. Commun.* **2015**, *51*, 8237–8240.

(S10) Tanaka, H.; Inoue, Y.; Mori, T., Circularly Polarized Luminescence and Circular Dichroisms in Small Organic Molecules: Correlation between Excitation and Emission Dissymmetry Factors. *ChemPhotoChem* **2018**, *2*, 386–402.